Time delay and microlensing research of the gravitationally lensed quasars.

by

Danuta Paraficz

supervised by

Jens Hjorth

MASTER THESIS

presented for the degree of

MASTER OF SCIENCE

University of Copenhagen

September 2006

Contents

1 Introduction

This master thesis is written at the University of Copenhagen and supervised by prof. Jens Hjorth. The thesis contains my theoretical and observational work on Gravitational Lensing. My work was based on observational data of the gravitational lens systems gathered at the Nordic Optical Telescope (NOT), La Palma. The two main purposes of this thesis are to analyze quasar microlensing effects and determine the time delay of the lensed system SDSS J0903+502.

The thesis is divided into four parts.

2 In this section I introduce the lensing theory so that the reader can follow and understand the work done for this thesis. I begin by presenting the history of microlensing and alternative methods for measuring dark matter. Then I show the methods for simple lens modeling and show what the visible lensing effects are. At the end I explain what the time delay in gravitationally lensed quasar is and the physics of quasars.

3 This section is based on a paper published in A&A and it introduces the main topics of quasar microlensing. On the beginning it is presented the history of microlensing and alternative methods for dark matter measurement. Further, it is shown how to obtain and analyze the microlensing signal in a lensed quasar light curve. At the end it is explained how the microlensing affects quasar spectra and how galaxy extinction influences the microlensing results.

4 In this section I present the observational part of my master thesis. I begin by explaining the difficulties involved in planning lensing observations and how one can overcome them. Then I review my monitoring program at the Nordic Optical Telescope (NOT). At the end I present the image reduction and deconvolution procedures and their implementation in gathered data.

5 This section presents the results of a half year of observations done at the Nordic Optical Telescope in the period October 2005 – April 2006. Here I present the analysis and conclusion from reduced and deconvolved images. At the beginning of this Chapter it is shown how the deconvolved images look and the astrometric and photometric results are presented. Next, I introduce the techniques and results of the SDSS J0903+502 lens modeling. At the end I present the light curve of the quasar images and its analysis.

2 Strong Lensing Theory

In this section I introduce the lensing theory so that the reader can follow and understand the work done for this thesis. I begin by presenting the history of microlensing and alternative methods for measuring dark matter. Then I show the methods for simple lens modeling and show what the visible lensing effects are. At the end I explain what the time delay in gravitationally lensed quasar is and the physics of quasars.

2.1 Historical background

The history of Gravitational Lenses (GL) begins with the beginning of modern physics. The first valuable scientific book (1704) "Opticks" contains basic GL ideas, its author – Sir Isaak Newton predicts that light rays can be bent by bodies.

This brilliant idea was forgotten for almost 3 generations. In the late seventeen hundreds, scientists came back to the subject with the idea of existence of black holes. "Black hole" (name invented much later) is an object so compact that it bents light in to a loop. Laplace (1795) gives the first equation for a critical radius of such a body. His equation is derived from the assumption that the body's escape velocity is equal to the light velocity:

$$R_{ms} = \frac{2GM}{c^2} \tag{1}$$

He also points out that black holes can be found by observing the behavior of objects moving in its vicinity.

Physicists inspired by Laplace's idea started studying the way celestial bodies affect light rays. An equation for the deflection angle was first introduced by J. Soldner (1804), he presents light as particles in the gravitational field and uses Newtonian mechanics to calculate deflection, giving:

$$\alpha = \frac{2GM}{V^2 r} \tag{2}$$

A big step forward in GL history was made by a famous physicist Albert Einstein. His general relativity theory gave the correct description of the behavior of light rays in a gravitational field. Einstein (1915) presents the equation for the deflection angle based on relativity and obtains a result which differs from "Newtonian" only by a factor of 2.

$$\alpha = \frac{4GM}{c^2 r} \tag{3}$$

Observers inspired by Einstein's paper, made the gravitational deflection measurements during the solar eclipse right after World War I. Although the observations (because of the lack of precision) did not rule out the Newtonian description, it made Einstein famous. The real proof was made 60 years later by use of radio-interferometer (Fomalont

& Sramek 1975). Since the time of Einstein, gravitational lensing gradually became of more interest to astronomers. The main question was if a lensing event is observable.

During a time of an extensive gravitational lens research astronomers also focused also on other important cosmological issues.

Shapley (1919) noted that galactic redshifts were positive, with the only exceptions being those in our own galactic neighborhood. Then, during the period 1923-24, Edwin Hubble discovered Cepheid variables in neighboring galaxies. These stars vary in light output in such a way that their intrinsic luminosity and the period of variability are linked. Measuring the period of variability can therefore in principle establish their intrinsic luminosity and hence their distance. Hubble used these stars to measure the distances to forty-two galaxies. Doing this he discovered that the observed redshifts were proportional to the distances. In 1929 he published the law of spectral displacements (Hubble 1929), which is now called Hubble‘s Law.

$$r = z/H_0 \tag{4}$$

Since the Hubble discovery the history of lensing is strongly related to the discovery of quasars.

The first quasar was discovered with radio telescopes at the end of the 1950s. Many were detected as radio sources with no corresponding visible object. In 1960, a radio source called 3C 48, was finally connected to its optical object. Astronomers detected what appeared to be a faint blue star at the location of the radio source and obtained its spectrum. Containing many unknown broad emission lines, the anomalous spectrum interpretation claimed by Bolton et al. (1963) of a large redshift was not generally accepted.

In 1962 another radio source, 3C 273, underwent five occultations by the moon. Measurements taken during one of the occultations allowed (Schmidt 1963) to optically identify the object and obtain an optical spectrum. This spectrum revealed the same strange emission lines. Schmidt (1963) discovered that that these were actually spectral lines of hydrogen redshifted at the rate of 15.8 percent, he showed that 3C 273 was receding at a rate of 47,000 km/s. This discovery revolutionized quasar observation and allowed other astronomers to find redshifts from the emission lines from other radio sources.

The word "quasar" is derived from quasi-star or a contraction of the more formal term quasi-stellar radio source. Later it was found that actually only 10% of quasars have strong radio emission. Hence the name 'QSO' (quasi-stellar object) is used to refer to these objects, including the 'radio-loud' and the 'radio-quiet' classes.

During 1960 the main topic was quasar high redshift and whether quasars were nearby or distant objects. One suggestion was, that the high redshift of quasars was not due to the Doppler effect but rather to light escaping from strong gravitational field. Although the shape of the continuous part of a quasar spectrum is very different from

any other stellar object. Quasar spectra possess no thermal spectrum, their spectra have no peaks (see Figure 13).

There were strong arguments against the idea of cosmologically distant quasars. One of them was that it implied energies that were far in excess of known energy conversion processes, including nuclear fusion. This objection was removed with the proposal of the accretion disc mechanism in the 1970s and today the cosmological distance of quasars is accepted by almost all researchers.

In the 1980s, models of quasars were developed. In these models, quasars were a class of active galaxies. In many cases it is simply the viewing angle that distinguishes them from other classes, such as blazars and radio galaxies. The huge luminosity of quasars is believed to be a result of friction caused by gas and dust falling into the accretion discs of supermassive black holes, which can convert about half of the mass of an object into energy.

This mechanism is also believed to explain why quasars were more common in the early universe, as this energy production ends when the supermassive black hole consumes all of the gas and dust near it. This means that it is possible that most galaxies, including our own Milky Way, have gone through an active stage (appearing as a quasar or some other class of active galaxy depending on black hole mass and accretion rate) and are now quiescent because they lack a supply of matter to feed into their central black holes to generate radiation.

Refsdal (1964), moves GL theory forward and establishes remarkable cosmological applications. Refsdal, inspired by both Einstein's and Hubble's great discovers, pointed out that if the lens is strong enough then the lensed source can be seen as a multiple images. Additionally if the source is variable (QSO) variations are observable in all the source images with some time delay from which Hubble constant can be calculated, as:

$$\Delta t \propto H_0^{-1}. \tag{5}$$

Finally Walsh et al. (1979) discovered the first gravitationally lensed system, QSO 0957+561, which appears to be a variable quasar with two counterparts separated by 6". Since that time enormous number of theoretical and observational GL publications came out and gravitational lensing became a major tool in astrophysics and cosmology (see Table 1).

Additionally to the GL by the galaxy, the light paths of the quasar images are affected separately by each object in the lensing galaxy. This effect is called "microlensing". The first quasar microlensing event was discovered 16 years ago by Irwin et al. (1989). But the history of microlensing analysis, begins earlier than its discovery, it begins with the seminal work of Refsdal (1966). Refsdal presents analysis of the theoretical brightness variation of a distant quasar as a single star passes through its beam. Initially, scientists considered microlensing as a magnitude variation caused by a single

Table 1: Time delays measured at optical wavelengths. The table shows the measured values: z_{ms}–redshift of source, z_{md} redshift of deflector(lens), $\theta_{\max}$ max angular image separations, $\Delta\tau$ – time delay.

Source	z_{ms}	z_{md}	$\theta_{\max}$	$\Delta\tau(Days)$	Reference
0957+561	1.41	0.36	$6\farcs1$	417±3	(Kundic et al. 1997)
PG 1115+080(C-A)	1.72	0.31	$2\farcs2$	9.4±3.4	(Schechter et al. 1997)
HE 1104-1805	2.32	0.73	$3\farcs2$	267±90	(Wisotzki et al. 1998)
B1600+434	1.59	0.41	$1\farcs4$	51±4	(Burud et al. 2000)
RX J0911.4+0551	2.80	0.77	$3\farcs1$	146±8	(Hjorth 2002)
SBS 1520+530	1.86	0.71	$1\farcs6$	130±6	(Burud et al. 2000)
HE 2149-2745	2.03	0.49	$1\farcs7$	103±24	(Burud et al. 2002)

object. But later it was proved that because of the big optical dept in a microlensing event, more than one object is involved.

The first person to perform a numerical simulation of the complex microlensing events was Young (1981). He shows how stars can affect the images of the quasar by introducing a complex variability. This was the first paper in history, where microlensing light curves were generated.

Paczynski (1986) work, significantly developed microlensing methods. He introduces a large number of microlensing events and describes numerical models of microlensing. Paczynski introduces a completely new method of microlensing analysis. His method is based on shooting with the rays through a regular grid of points in the image plane. Using this method he was then able to calculate positions of quasar images.

A big improvement was achieved with the ray-shooting method introduced by Kayser (1986) and Schneider & Weiss (1988), which does not attempt to find the images of point sources, but instead calculates rays on a grid in the lens plane, obtaining a map of the magnification in the source plane.

Light coming from sources, especially from distant ones, is influenced by dust along the its path. This is a well known fact, which has been taken into account for years by astronomers measuring astrophysical and cosmological parameters. Extinction changes most of the measurements, it influence Hubble Constant estimation (Freedman et al. 1998), the cosmological model using Ia supernovae (Perlmutter et al. 1997) and gravitational lens modeling (Kochanek 1996).

The first idea to use gravitationally lensed quasars as a probe for the extinction curves in high redshift galaxies was given by Nadau et al. (1991). Astronomers inspired by Nadau started looking for extinction in the distant galaxies. In most of the galaxies extinction appears to by detectable (Falco 1999) but extinction curves were very different from that of the Milky Way

The Hubble constant and dark matter have recently become of major interest among

astronomers. GL gives an alternative insight to those two issues, which is why it became a powerful astrophysical tool.

2.1.1 Previous work on SDSS J0903+502

The second part of this master thesis is based on the observations of a doubly lensed quasar SDSS J0903+502, which discovery as first reported by Johnston et al. (2003). It was discovered from the Sloan Digital Sky Survey targeted for SDSS spectroscopy as a luminous red galaxy, although the spectra showed existence of a quasar at z$\simeq$3.6. Further research, photometric and spectroscopic survey at the Apache Point Observatory in New Mexico (York et al. 2000) and one night spectroscopy and imaging on the Keck II telescope gave information about SDSS J0903+503 physical properties.

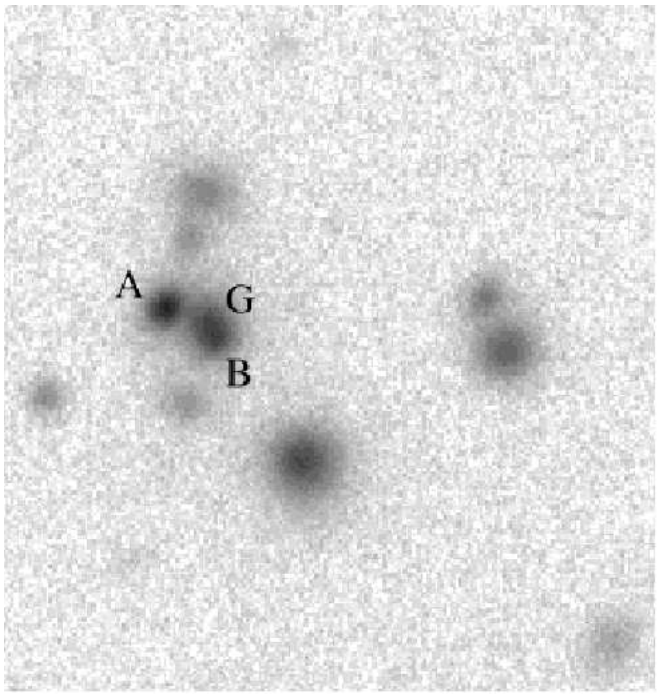

Figure 1: SPIcam r-band image of the area around SDSS J0903+502. The two quasar images and the galaxy are labeled A, B and G respectively.

Using these observations, Johnston et al. (2003) estimated the positions and the magnitudes of both quasar images and the galaxy in i and r-band (see Table 2).

Johnston et al. (2003) also modeled the lensing galaxy. Assuming that the lens is an isothermal singular sphere he obtained that ellipticity ϵ=0.47 at an angle $\theta_\epsilon = 4°.6 \pm 2.8$, giving a time delay of $\Delta t = 67.4 \pm 2.8$ days.

Object	R.A.	Decl.	r mag	i mag
QSO A	09 03 35.132	+50 28 20.21	19.99±0.01	19.43±0.01
QSO B	09 03 34.877	+50 28 18.75	20.78±0.03	20.27±0.05
Galaxy	09 03 34.925	+50 28 19.53	19.59±0.02	18.86±0.04

Table 2: ARC Photometry model results

2.2 The point-like deflector.

According to Einstein's principle, an object which possesses mass changes the shape of space time in its vicinity. Therefore, the deflection of a light beam by a massive object, is really caused by the light beam moving along a geodesic in the locally curved space-time.

The goal of this section is to find out how light is deflected on massive bodies.

Equation 6 is a full description of the light path in spherically symmetric gravitational field for an arbitrary distance from the deflector:

$$\phi_{\min} - \phi_{\text{infty}} = \int_0^1 \frac{dx}{\sqrt{1 - x^2 - \frac{2GM}{r_{\min}}(1 - x^3)}}. \tag{6}$$

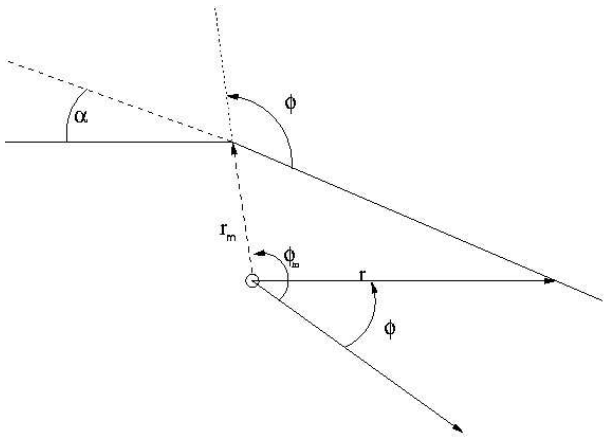

Figure 2: Light beam deflected by a massive object, where α is the deflection angle and $r_{\min}$ is the minimum distance.

Approximations. When we expand equation 6 to first order, then the deflection angle equals:

$$\tilde{\alpha} = \frac{4GM}{r_{\min}}. \tag{7}$$

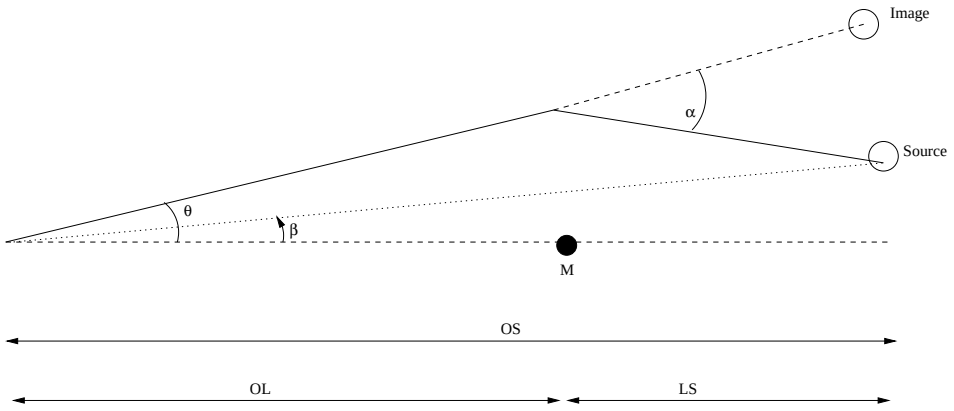

Figure 3: The figure shows the position angle of the image (θ) and the original source (β), along with the deflection angle (α). OS, OL and LS are the angular diameter distances from the observer to the source, the observer to the lens, and the lens to the source respectively.

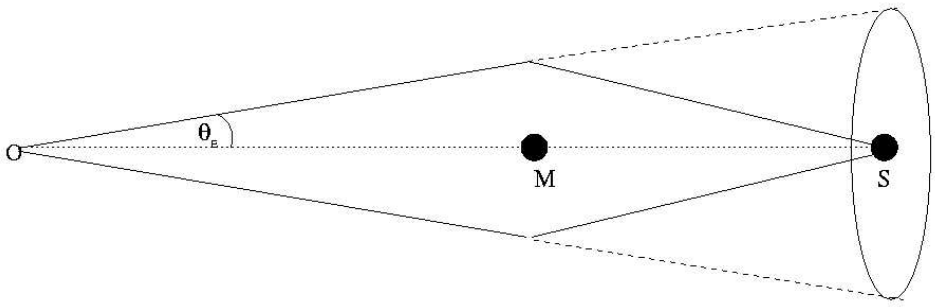

Figure 4: An Einstein ring is formed when the source (S) is perfectly aligned with the lens (L) and the observer (O).

This configuration is shown on Figure 2. From simple geometry of the system (see Figure 3) we know that:

$$\theta D_{\rm OS} \simeq \beta D_{\rm OS} + \tilde{\alpha} D_{\rm LS} \tag{8}$$

where $\tilde{\alpha}$ is given by the equation:

$$\alpha = \tilde{\alpha} \frac{D_{\rm LS}}{D_{\rm OS}}. \tag{9}$$

Lens equation. Now when we know the deflection angle of the light, we will write the relation between the source and image positions, which is called lens equation. We can obtain the lens equation by putting equation 9 in to equation 8:

$$\theta \simeq \beta + \alpha. \tag{10}$$

This equation is not so useful since we can observe only one variable, θ and the other two, β and α, are unknown, thus, we rewrite α as:

$$\alpha = \frac{D_{\mathrm{LS}}}{D_{\mathrm{OS}}} \frac{4GM}{r_{\mathrm{min}}} \tag{11}$$

and from Figure 2 and Figure 3 we see that $r_{\mathrm{min}} = \theta D_{\mathrm{OL}}$ so :

$$\alpha = \frac{D_{\mathrm{LS}}}{D_{\mathrm{OS}} D_{\mathrm{OL}}} \frac{4GM}{\theta}. \tag{12}$$

Now the lens equation as the form:

$$\theta^2 - \beta\theta - \theta_{\mathrm{E}}^2 = 0 \tag{13}$$

where θ_{E} is the "Einstein radius" described by the equation:

$$\theta_{\mathrm{e}} = \sqrt{\frac{D_{\mathrm{LS}}}{D_{\mathrm{OS}} D_{\mathrm{OL}}} 4MG}. \tag{14}$$

The *Einstein radius*, θ_{E}, is the radius of the ring, so called "Einstein ring", which is created when the source is aligned with the observer and the lens (see Figure 4).

This description is only valid for models assuming point-like lenses and point-like sources.

2.3 Extended lenses

From the previous chapter we have learned about the physics of a point like lens but in most the cases lens is not a point but has an extended mass distribution. To understand the method used to measure the Hubble constant we need to know the mathematical description of extended lenses.

The problem of extended lenses is very complex so in this chapter I will try only briefly show how one can calculate the deflection due to an extended mass.

2.3.1 Theory

In the case where a lens is not a point we have to, instead of a point mass – M, use a surface mass density – $\Sigma(\vec{\xi})$:

$$\Sigma(\vec{\xi}) = \int dr \rho(\vec{\xi_1}, \vec{\xi_2}, \vec{\xi_3}) \tag{15}$$

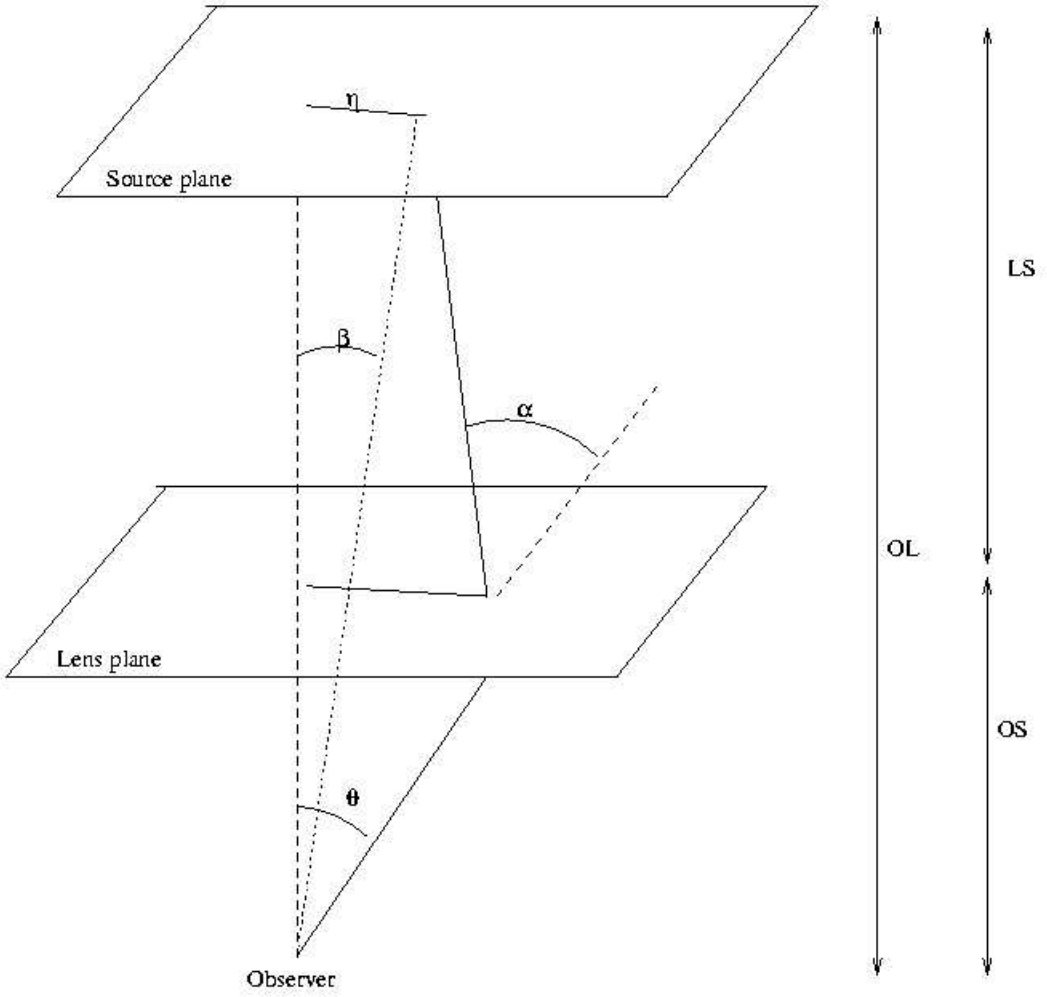

Figure 5: The deflection of light by an extended lens, where ξ is a coordinate on a lens plane and η is a coordinate on a source plane.

where r is the direction of the observer-lens line, ρ is the spatial density and $\vec{\xi_1}, \vec{\xi_2}, \vec{\xi_3}$ are the arbitrary space variables. Now the deflection angle have form:

$$\alpha = 4G \int d^2\xi' \Sigma(\vec{\xi'}) \frac{\vec{\xi} - \vec{\xi'}}{|\vec{\xi} - \vec{\xi'}|^2}. \tag{16}$$

We can see from Figure 5 that:

$$\vec{\theta} = \vec{\xi} D_{\mathrm{OL}} \tag{17}$$

By introducing equation 16 with new variable θ, we obtain the deflection angle for extended mass new form:

$$\alpha(\theta) = \frac{1}{\pi} \int d^2\theta' \kappa(\theta') \frac{\theta - \theta'}{|\theta - \theta'|^2} \tag{18}$$

where: $\kappa(\theta)$ is the dimensionless surface mass density given by equation:

$$\kappa(\theta) = \frac{\Sigma(D_{\mathrm{OL}}\theta)}{\Sigma_{\mathrm{cr}}} \tag{19}$$

Σ_{cr} is the critical surface mass density, given by equation:

$$\Sigma_{\mathrm{cr}} = \frac{1}{4\pi G} \frac{D_{\mathrm{OS}}}{D_{\mathrm{OL}} D_{\mathrm{LS}}}. \tag{20}$$

It is also convenient to represent the deflection angle in terms of a projected gravitational potential:

$$\psi(\vec{\xi}) = 2G \int d^2\xi' \sum(\vec{\xi'}) ln|\vec{\xi} - \vec{\xi'}| \tag{21}$$

So the deflection angle is:

$$\vec{\alpha}(\vec{\xi}) = 2\Delta_\xi \psi(\vec{\xi}) \tag{22}$$

Having equation 22 we can find the rescaled projected gravitational potential:

$$\Psi = 2 \frac{D_{\mathrm{LS}}}{D_{\mathrm{OS}} D_{\mathrm{OL}}} \psi \tag{23}$$

and now we can rewrite the lens equation in the simple form:

$$\vec{\beta} = \vec{\theta} - \vec{\Delta_\theta} \Psi(\vec{\theta}). \tag{24}$$

As we see from equation 24 in order to calculate the real position of a source, one has to know the mass distribution of the lens. In the case of gravitationally lensed quasars, the mass distribution of deflectors is never accurately known, as there are no direct observations which allow us to accurately measure it. Thus, in order to calculate the lens equation for extended lens one has to create mathematical model of mass distribution. Those models are described in the next sections.

2.4 Power-law lenses

The mass distribution models described in this section are rather simple but they are still applicable to real lensing systems.

2.4.1 Theory

For simplicity we can assume that the deflectors (high redshift galaxies) are circularly symmetric. This assumption simplifies the calculation, reducing it to the power-law analysis.

When the lens has the circularly symmetric density distribution, $\rho \propto r^{-n}$, then the deflection angle is given by:

$$\alpha(\theta) = b\left(\frac{\theta}{b}\right)^{2-n} \tag{25}$$

and the dimensionless surface mass density – the convergence is:

$$\kappa(\theta) = \frac{3-n}{2}\left(\frac{\theta}{b}\right)^{1-n} \tag{26}$$

where n is the power index and b, is the deflection scale.

2.4.2 Point-like lens

For the limit $n \to 3$, we get a point-like lens, and b becomes:

$$b = \sqrt{\frac{D_{\rm OS}D_{\rm OL}}{D_{\rm LS}}4MG} \tag{27}$$

and the deflection angle is given by equation:

$$\alpha = \frac{b^2}{\theta} \tag{28}$$

and the convergence is simply: $\kappa = 0$.

2.4.3 Isothermal lens

For n=2, we get the isothermal lens, and b is given by:

$$b = \sigma D_{\rm OS}D_{\rm OL}4\pi \tag{29}$$

where: σ – is the velocity dispersion of the lens, the deflection angle is: $\alpha = b$, and the convergence is:

$$\kappa = \frac{b}{2\theta}. \tag{30}$$

2.5 Lensing effects

In this section we apply the lens equation to simple mass models to the lens equation in order to observe the lensing effects, i.e., the change of the image positions, magnifications (see also Appendix D) and distortion.

2.5.1 Images

Point-like lens. In the case of the point-like lens, the lens equation has the form:

$$\theta^2 - \beta\theta - \theta_{\mathrm{E}}^2 = 0 \tag{31}$$

This equation has two solutions, the images appear on the opposite sides of the lens with separation:

$$\Delta\theta = \theta_+ - \theta_- = 2\theta\sqrt{1 + \frac{\beta^2}{4\theta_{\mathrm{E}}^2}} \geq 2\theta_{\mathrm{E}}. \tag{32}$$

Isothermal lens. The Singular Isothermal Sphere (SIS) model has the dimensionless surface mass density given by:

$$\kappa(\theta) = \frac{1}{2}\frac{\theta_{\mathrm{E}}}{\theta}. \tag{33}$$

and when we apply the lens equation, (24), we get two solutions:

- If $\beta < \theta$, we get two images:

$$\theta = \beta + \theta_{\mathrm{E}}\beta \tag{34}$$

$$\theta = \beta - \theta_{\mathrm{E}}\beta \tag{35}$$

- If $\beta > \theta$, we have only one image:

$$\theta = \beta + \theta_{\mathrm{E}}\beta \tag{36}$$

From equations 34 and 35 we see that $\Delta\theta = const$, which is an important feature of isothermal lenses.

2.5.2 Source distortion

In the previous sections we did not consider what happens if a source is not just a point but has some angular distribution of brightness. Now we will examine how such an object will be magnified by different lenses.

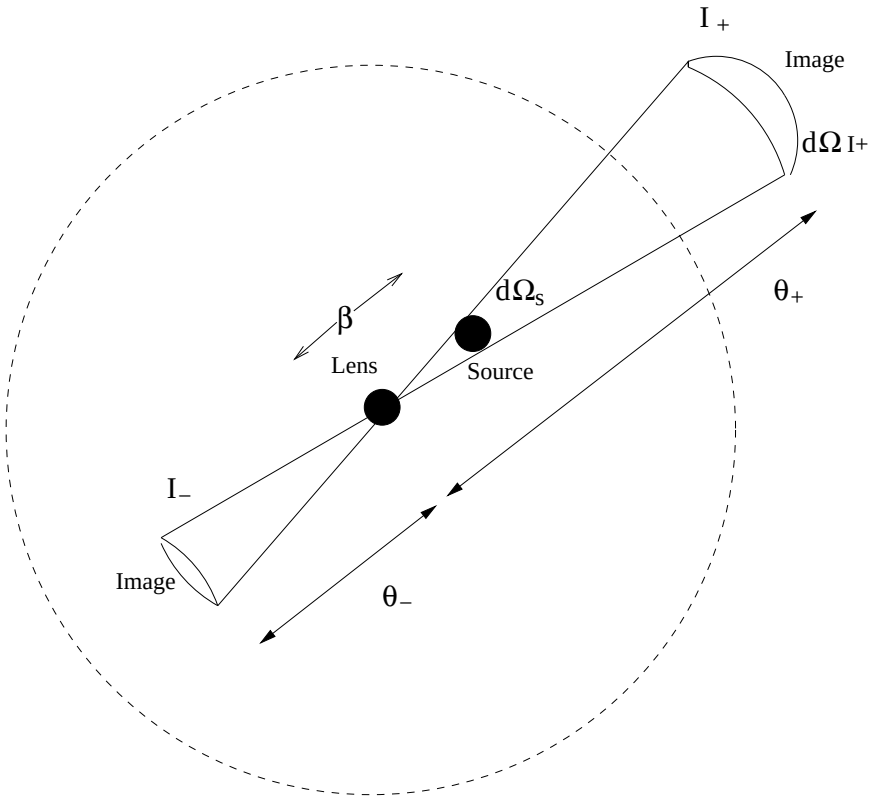

Figure 6: Magnified images of a source lensed by a point mass. The dashed circle is the Einstein ring. The solid angle of the source $d\Omega$ is magnified in the lens plane to $d\Omega_+$ and $d\Omega_-$ for the two images.

Point like lenses Let us first consider a point-like lens and a source with an angular position $\vec{\beta}$, with this setup there are two images of the source seen by an observer in angular positions θ_+ and θ_- given by equation 13.
The solid angle of a source is given by equation:

$$d\Omega_0 = \frac{dS}{D_{\rm OS}^2} = \beta d\phi d\beta \tag{37}$$

and its images are distorted accordingly:

$$d\Omega_\pm = \frac{dS_\pm}{D_{\rm OL}^2} = \beta_\pm d\phi d\theta_\pm \tag{38}$$

and knowing the equations 37 and 38, we obtain the amplifications of source images:

$$A_\pm = \frac{d\Omega_\pm}{d\Omega_0} = \frac{\theta_\pm d\theta_\pm}{\beta d\beta} = \frac{1}{2} \pm \frac{\beta^2 + 2\theta_{\rm E}^2}{2\beta\sqrt{\beta^2 + 4\theta_{\rm E}^2}}. \tag{39}$$

2.5.3 Extended lenses

For the extended mass distribution, we use the two dimensional vector of deflection, $\vec{\alpha}$ (equation 18). To obtain the magnification we use the Jacobian which is maps between a source and an image:

$$A_{\rm ij}(\theta) = \frac{\partial \beta_i}{\partial \beta_j} = \left(\delta_{\rm i,j} - \frac{\partial^2 \Psi}{\partial \theta_i \partial \theta_j}\right) \tag{40}$$

then $A_{\rm ij}(\theta)$ is equal to:

$$\tilde{\mathbf{A}} = \begin{pmatrix} 1-\kappa-\gamma_1 & -\gamma_2 \\ -\gamma_2 & 1-\kappa+\gamma_1 \end{pmatrix} \tag{41}$$

where γ is the shear given by equations:

$$\gamma_1 = \frac{1}{2}\left(\frac{\partial^2 \Psi}{\partial \theta_1^2} - \frac{\partial^2 \Psi}{\partial \theta_2^2}\right). \tag{42}$$

$$\gamma_2 = \frac{\partial^2 \Psi}{\partial \theta_1 \partial \theta_2} \tag{43}$$

Now we can define the amplification for an extended lens mass:

$$A = (det\tilde{A})^{-1} = \frac{1}{(1-\kappa)^2 - \gamma^2} \tag{44}$$

where: $\gamma = \sqrt{\gamma_1^2 + \gamma_2^2}$.

2.5.4 Circular lenses- power-law

Shear for circular lenses with a power law distribution is given by:

$$\gamma(\theta) = \frac{n-1}{2}\left(\frac{\theta}{b}\right)^{1-n}. \tag{45}$$

Magnification of source images in power-law model is:

$$A_{\pm} = 1 - \kappa \pm \gamma. \tag{46}$$

To get the shear profiles and magnifications for a specific model of a circular lens we simply substitute equations 46 by any of a shear with a circular symmetry lens described in Section 2.4.

2.6 Critical and caustics lines

In order to visualize how images are placed and distorted we define some specific curves.

- Critical curves – the curves in the lensing plane corresponding to infinite magnification. They are closed and smooth curves which satisfy the condition: $A(\theta) = 0$
- Caustic lines – are the critical curves mapped into the source plane by use of the lensing equation.

Figures (7 – 9) show examples of caustic and critical lines. The left hand-side figures show positions of the sources and caustic lines which divide the fields into 3 regions from where a source produces 1, 3 or 5 images. The right hand-side figures show positions of images and critical lines.

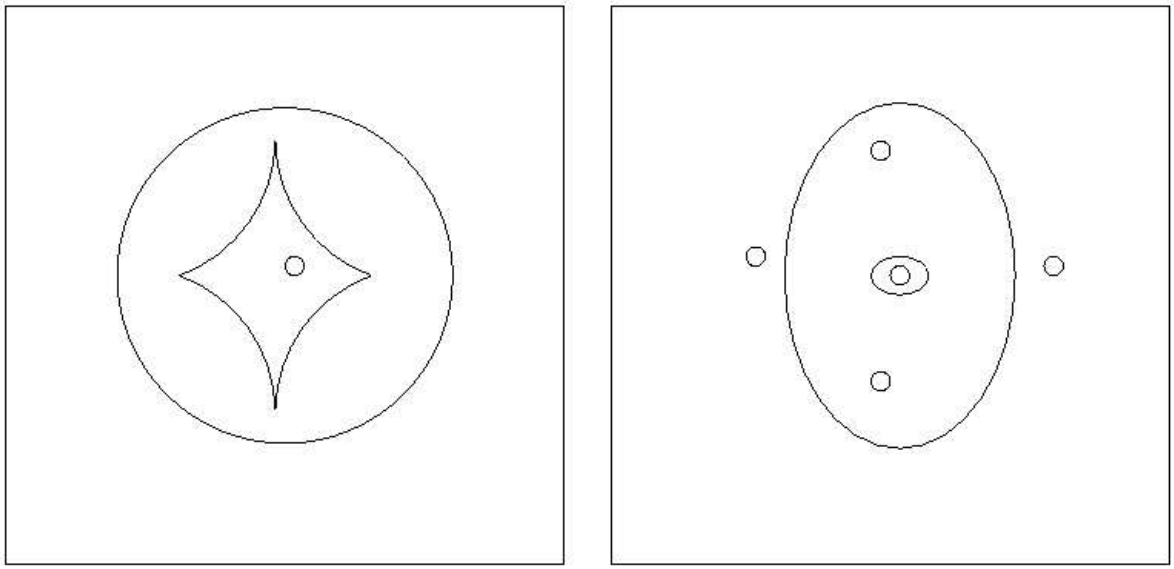

Figure 7: **Left**: The source is near the center of the inner caustic line. **Right**: The source position causes the creation of the 5 symmetrically aligned images.

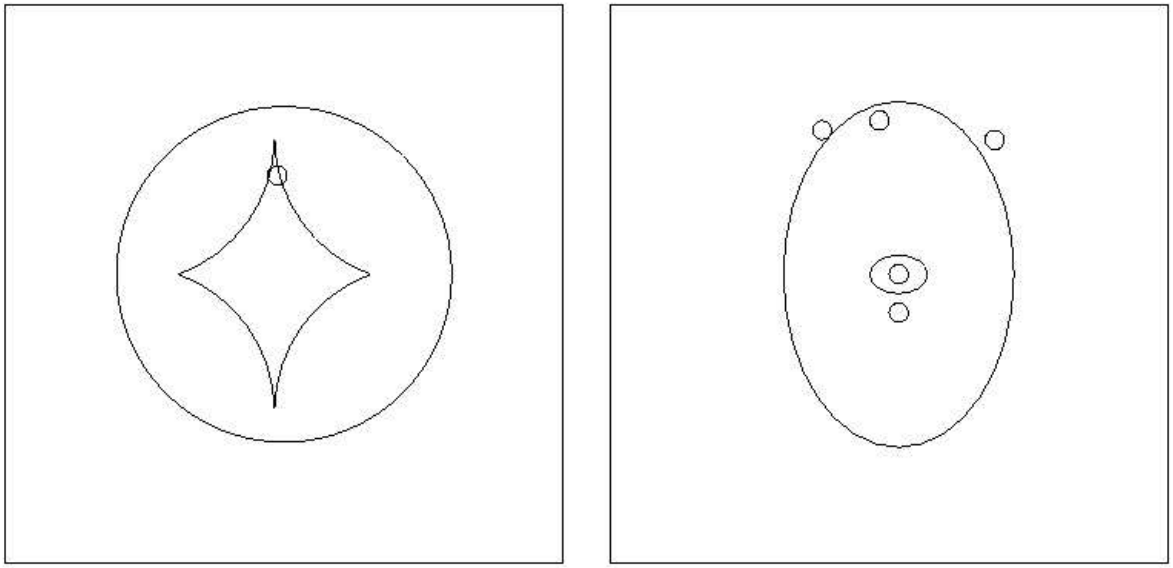

Figure 8: **Left**: The source is in the top corner of the inner caustic line. **Right**: The source position causes the creation of 5 images.

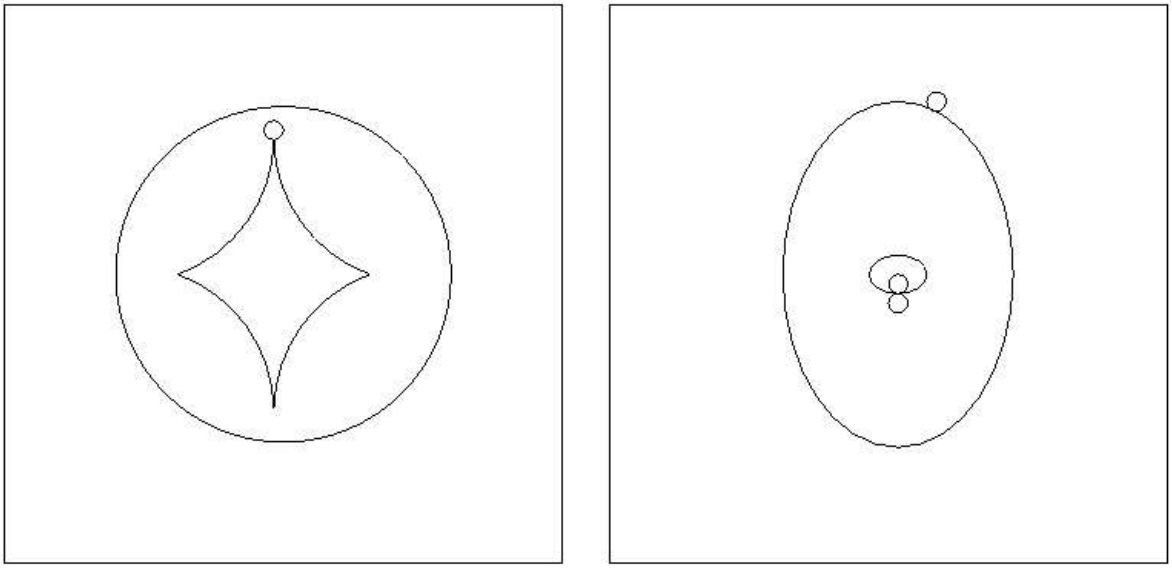

Figure 9: **Left**: The source is above the top corner of the inner caustic line. **Right**: The source position causes the creation of 3 images.

2.7 Time delay

When a GL source, a quasar, has an intrinsic variability due to some physical process, this variability can be seen in all the images. Because of the two time delay factors,

geometrical and gravitational, quasar intrinsic variability shows up in the images at different times. A description on what is a Hubble constant and how one can calculate it using the time delay is given in the Appendices A and B respectively.

2.7.1 Gravitational time delay

The gravitational time delay occurs because a gravitational field affects space–time. To obtain an equation for the gravitational time delay one has to consider radial motion ($d\phi = 0$) in the Schwarzschild metric (see Appendix C). First we introduce the Schwarzschild metric:

$$ds^2 = \left(\frac{1 - GM/2R}{1 + GM/2R}\right) dt^2 - \left(1 + \frac{GM}{2R}\right)^4 (dx^2 + dy^2 + dz^2) \tag{47}$$

where:

- $r = R(1 + GM/2R)$
- $x = R \sin\theta \cos\Psi$
- $y = R \sin\theta \sin\Psi$
- $z = R \cos\theta$

In the Newtonian limit, where gravity is weak, we have:

$$ds^2 = (1 + 2\Psi)dt^2 - (1 - 2\Psi)(dx^2 + dy^2 + dz^2) \tag{48}$$

were: $\Psi = GM/R$.

For light, ds=0 and assuming that light propagates along the z axis we get:

$$\frac{dt}{dz} = (1 - 2\Psi). \tag{49}$$

We integrate equation 49 and get:

$$t_2 - t_1 = \int_{z_1}^{z_2} (1 - 2\Psi). \tag{50}$$

Finally we obtain that the gravitational part of the time delay is given by:

$$\delta t_{\text{grav}} = -2 \int_{z_1}^{z_2} \Psi(z) dz. \tag{51}$$

2.7.2 Geometrical time delay

The geometrical part of the time delay occurs because the light paths from both sources have different lenght, so from a simple geometry we get:

$$\delta t_{\rm geom} = -\frac{D_{\rm OS} D_{\rm OL}}{2 D_{\rm LS}} (\vec{\theta}\vec{\beta})^2. \tag{52}$$

.

2.7.3 Time delay in an expanding Universe

The time delays obtained in the previous sections where for close by sources, thus, if we also want to consider the time delay for distant objects we have to include also the expansion of the Universe were all photons are redshifted. The final equation for time delay in an expanding Universe is:

$$\delta t = (1 - z_{\rm L}) \frac{D_{\rm OS} D_{\rm OL}}{D_{\rm LS}} \left(\frac{1}{2} (\vec{\theta} - \vec{\beta})^2 - \Psi \right) \tag{53}$$

where:

$z_{\rm L}$ – is the redshift of the lens.

Thus, in order to obtain the Hubble constant from a time delay observation we need to know the distances to both the lens and the source and the mass distribution of the lens.

If we do not have any direct measurement of the distances to the lens and the source, which is often the case, we need to calculate it. Calculation of the distances introduces additional error into the time delay estimation because it requires prior knowledge of the cosmological constants. One can calculate the approximate distance to an object using:

$$D(z) = \frac{1}{1+z} \begin{cases} R_{\rm H} \frac{1}{\sqrt{1-\Omega_m-\Omega_\Lambda}} \sinh[\sqrt{1-\Omega_m-\Omega_\Lambda} I(z)] & for \quad \Omega_m + \Omega_\Lambda < 1 \\ R_{rmH} I(z) & for \quad \Omega_m + \Omega_\Lambda = 1 \\ R_{\rm H} \frac{1}{\sqrt{1-\Omega_m-\Omega_\Lambda}} \sin[\sqrt{1-\Omega_m-\Omega_\Lambda} I(z)] & for \quad \Omega_m + \Omega_\Lambda > 1 \end{cases} \tag{54}$$

where:

- $R_{\rm H} = c/H_0$ is the Hubble radius
- I(z) is an integral $I(z) = \int_0^z [f(z)]^{-1} dz$ of the function $f(z)$:

$$f(z) = \sqrt{\Omega_m (1-z)^3 + (1 - \Omega_m - \Omega_\Lambda)(1-z)^2 + \Omega_\Lambda} \tag{55}$$

- $z_{\rm S}$ – redshift of the source,

- z_{L} – redshift of the lens,
- Ω_m – energy density of matter in the Universe,
- Ω_Λ – vacuum energy density in the Universe.

From direct observations we can get z_{S} and z_{L} but Ω_m and Ω_Λ are unknown. Estimation of this constants can change significantly time delay.

Recent observations of the CMB (Cosmic Microwave Background) and redshifts of galaxies gave evidence for space being flat with density parameters $\Omega_m = 0.3$, $\Omega_\Lambda = 0.7$.

The main uncertainty in the time delay calculations comes from lenses modeling.

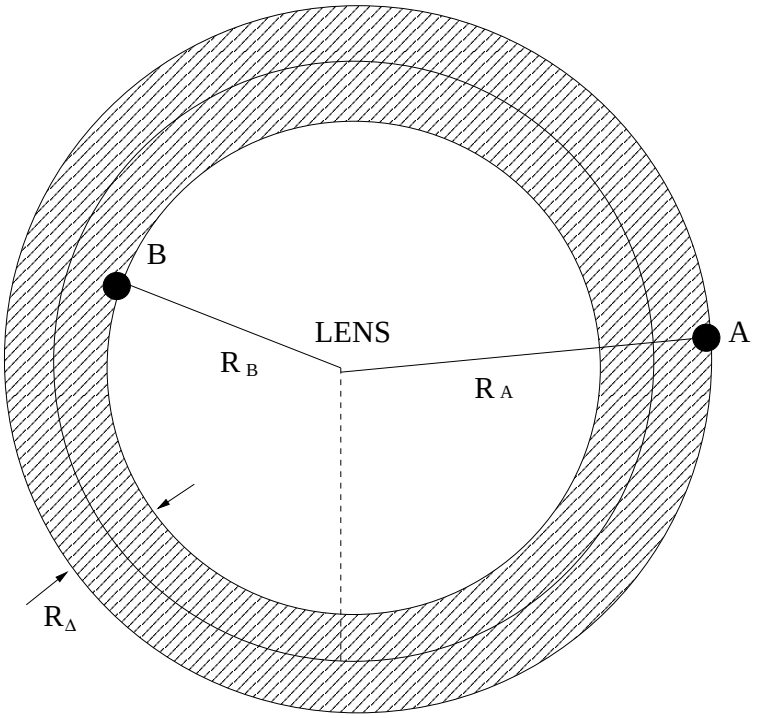

Figure 10: Diagram of a two-image time delay lens. The lens lies at the origin, with the two images A and B at radii R_a and R_{B} from the lens center. The images define an annulus of average radius $\langle R \rangle = (R_{\mathrm{A}} - R_{\mathrm{B}})$ (Schechter 2003).

If a given lens can be approximated by a power law (section 2.4) then the time delay between the two images can be described by (Schechter 2003):

$$\Delta t = 2\Delta t_{\mathrm{SIS}} \left[1 - \langle \kappa \rangle - \frac{1 - n\langle \kappa \rangle}{12} \left(\frac{\Delta R}{\langle R \rangle} \right)^2 + o\left(\left(\frac{\Delta R}{\langle R \rangle} \right)^3 \right) \right] \tag{56}$$

where:

- $\langle\kappa\rangle$ – is the mean surface density between the two images Δt_{SIS} – is the time delay for a singular isothermal sphere model of the lens given by equation:

$$\Delta t_{\mathrm{SIS}} = \frac{1}{2}\frac{D_{\mathrm{OL}} D_{\mathrm{OS}}}{D_{\mathrm{LS}}}(R_{\mathrm{A}}^2 - R_{\mathrm{B}}^2) \propto H_0^{-1} \tag{57}$$

  where R_{A} and R_{B} are the radii of the two co-linear images

  - $R_{\mathrm{A}} = |\vec{\beta}| + b$
  - $R_{\mathrm{B}} = |\vec{\beta}| - b$
  - and $b = 4\pi D_{\mathrm{OS}} D_{\mathrm{OL}} \sigma^2$

2.8 QUASi-stellAR radio sources

Before introducing dark matter measurements, it is essential to explain the nature of quasars, the sources in the strong gravitational lensing events. This section contains the history of the discovery of quasars and explains their known physical properties.

2.8.1 Definition of QSO

According to the Encyclopedia, a quasar (contraction of QUASi-stellAR radio source) is an astronomical source of electromagnetic energy at very high redshift. In optical wavelengths, a quasar is a point source. The general consensus is that this high redshift is cosmological, a result of Hubble's law, which implies that quasars must be very distant and hence very luminous.

More than 60 000 quasars are presently known. All observed spectra have shown considerable redshifts, ranging from 0.06 to the recent maximum of 6.4, most quasars are known to lie at a distance of 1.0 Gpc or more. Quasars are found to vary in luminosity in differing time periods, they vary in brightness every few months, weeks, days or hours. The time scale of the variability indicates that quasars cannot be larger than a few light weeks.

Scientists claim that quasars are probably small active galaxies, which are powered by super-massive black holes (see Figure 11).

2.8.2 Quasar Spectra

Quasars have a non-thermal spectrum. They have about the same power at all wavelengths down to the microwave wavelengths. The spectrum looks like the synchrotron radiation from charged particles spiraling around magnetic field lines at nearly the speed of light (see Figure 13).

There are a few features distinguishing quasar spectra:

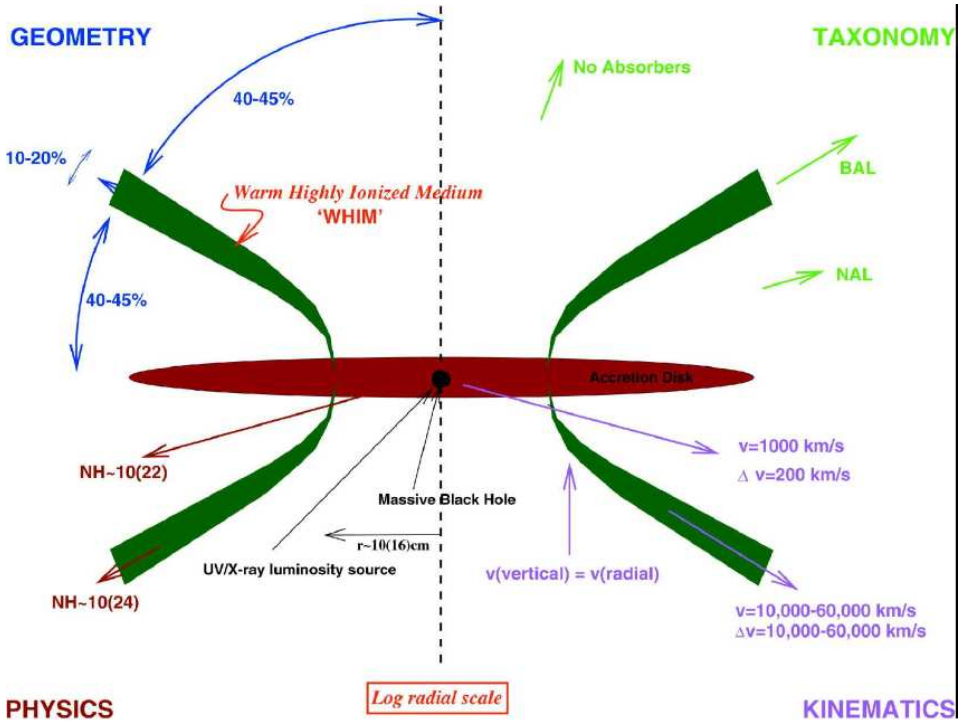

Figure 11: Structure of a QSO – Elvis (2000)

- characteristic strong emission lines rising above a broad continuum (see Figure 12),
- the emission lines are highly shifted, indicating that quasars are high redshift phenomena (see Figure 14),
- no absorption lines.

The Lyman-alpha forest indicates that the intergalactic medium has undergone re-ionization into plasma, and that neutral gas exists only in small clouds. The other interesting characteristic of quasars is that they show evidence of elements heavier than helium. This is taken to mean that galaxies underwent a massive phase of star formation creating population III stars between the time of the Big Bang and the first observed quasars.

The size of quasars are known from quasar spectra studies (see Figure 12). From the time-scales variability one can estimate an upper limit on the size. In most quasars the variability has been found to be of the order of weeks or days, which sets an upper limit of a few light weeks.

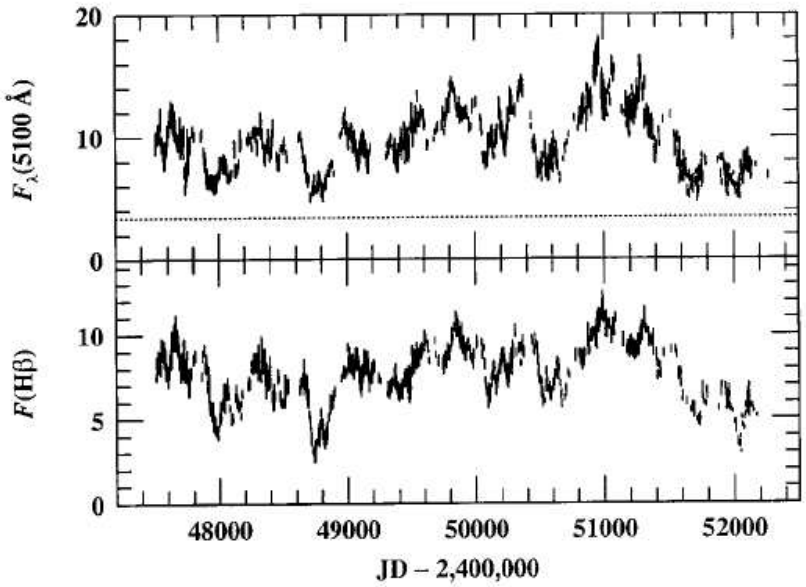

Figure 12: A variability of the continuum and spectral lines in NGC 5548.*First*: The UV continuum. *Second*: IUE-FES 5500$\dot{A}$.

3 Microlensing – dark matter measurements

The term "microlensing" describes magnitude variations of a background source caused by foreground compact objects (stars, planets). The quasar microlensing is a very efficient tool for dark matter measurements. This section is based on a paper published in A&A (see Appendix E) and it introduces the main topics of quasar microlensing. On the beginning it is presented the history of microlensing and alternative methods for dark matter measurement. Further, it is shown how to obtain and analyze the microlensing signal in a lensed quasar light curve. At the end it is explained how the microlensing affects quasar spectra and how galaxy extinction influences the microlensing results.

3.1 Other methods for measuring the Dark Matter in Universe

From cosmic microwave background surveys like COBE and WMAP astronomers have proved that the Universe is flat. This is a revolutionary discovery because the matter we observe is not sufficient to create flat space. Therefore, scientist are aware of, that what we see is only a small fraction of what actually exists.

One of the methods for studying dark matter is observing distant object. In 1970 astronomers made observations of many galaxies in order to measure the rotation curves. They discovered that the velocity does not decrease with the radius as it does in the

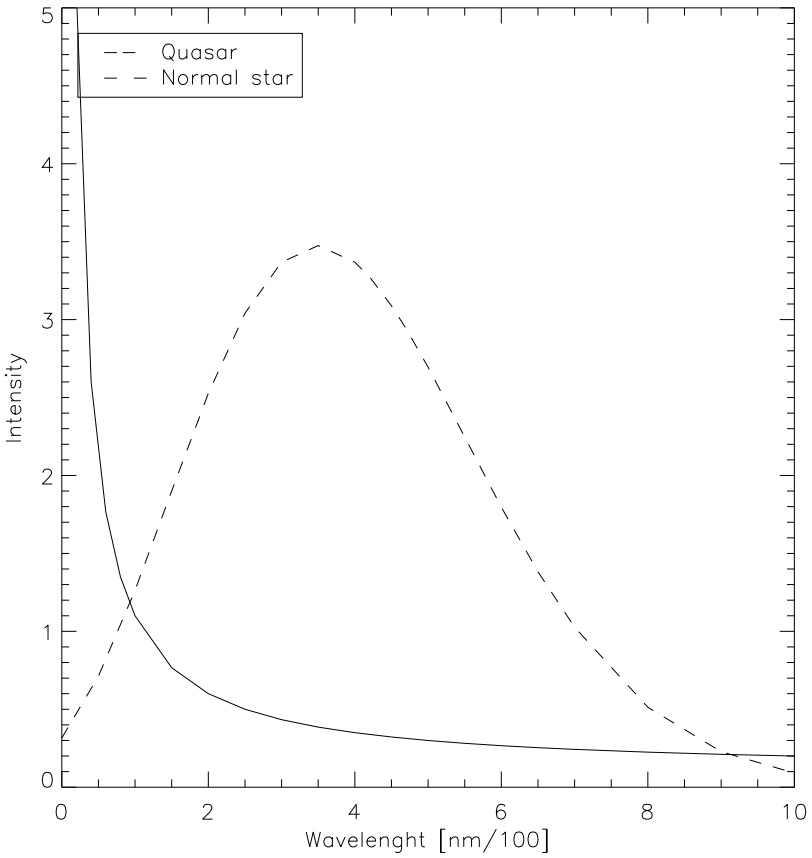

Figure 13: Quasars have a decidedly non-thermal spectrum: they are luminous in the X-rays, ultraviolet, visible, infrared, and radio bands. They have about the same power at all of the wavelengths down to the microwave wavelengths. The spectrum looks like the synchrotron radiation from charged particles spiraling around magnetic field lines at nearly the speed of light.

solar system, the rotation velocity of galaxies is constant at large radii (Shalyapin 1993).

According Kepler law:

$$\frac{GM(r)}{r^2} = \frac{v(r)^2}{r} \tag{58}$$

the gravitational force, $\frac{GM(r)}{r^2}$, is balanced by the centrifugal force, $\frac{v(r)^2}{r}$, and if the velocity, $v(r)$, is constant, then the mass must scale with the radius, $M(r) \propto r$. Hence, since the rotation curves of the galaxies are flat, their mass must be growing with the radius.

The observations in Hα of the dust clouds surrounding galaxies shows that even

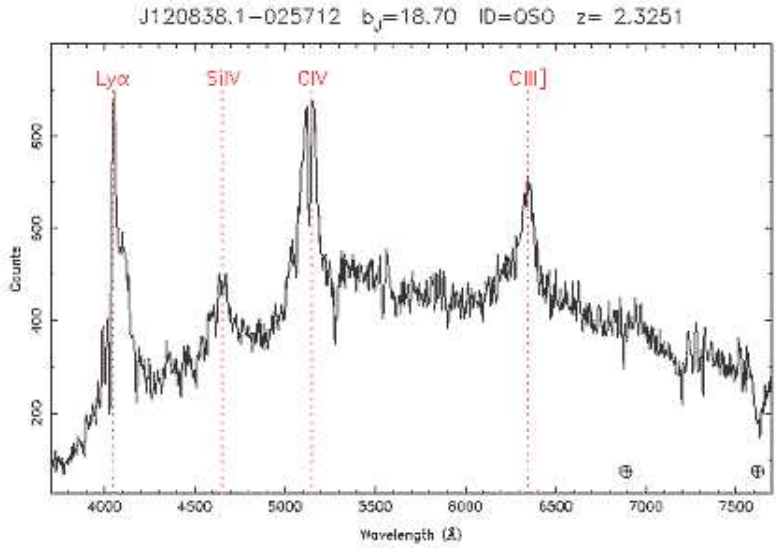

Figure 14: The typical spectra of QSOs in the UV spectral range (Reichard 2003).

outside the galaxy where the stars are no longer visible, the rotation curve is still constant, which means that more then 90% of the galactic mass is unknown and invisible. Results from both galaxy rotation curve and CMB measurements make dark matter research a major subject of Cosmology.

3.2 Microlensing extraction

The microlensing effect appears when one of the light path passes nearby a compact object in the lens galaxy, thus a microlensing event affects only one of the light paths.

The observed magnitude changes of the quasar images are due to: brightness changes of a quasar itself, galaxy lensing and microlensing. Additionally all brightness changes can have the same order of time scale and magnification, which makes both time delay and microlensing measurements difficult.

In order to analyze a quasar light curve one should separate the effects which influence quasar images. The most useful information for doing so is that intrinsic variability of quasars appears in both images. As we have learned from previous section it appears with some time delay, which length depends on the source-lens-observer geometry and lens mass.

Thus, the first step for separating the influence of different events is to find the time delay of the system (see Section 2.10). The next step is to shift all the data from one of the images by the calculated delay. After shifting, the variability which appear at the same rate and time in both images is the intrinsic variation of the quasar.

In order to remove effects of intrinsic variations of a quasar from light paths it is common to calculate the light paths difference. To get proper light curve difference one has to make a transformation of one of the light curves:

$$a = \frac{A_i - A_{i+1}}{t_i - t_{i+1}} \tag{59}$$

$$b = \frac{1}{2}(A_i + A_{i+1} - a(t_i + t_{i+1})) \tag{60}$$

$$A_i^{transf} = at_i + b \tag{61}$$

$$C(i) = \sum_i A_i^{transf} - B_i \tag{62}$$

Once one has shifted and subtracted the two images, only the microlensing variation remains, (see Figure 15).

3.3 Microlensing light curve interpretation

The length of a microlensing event is directly dependent on the lens mass. Thus, if one has the time scales of the events, one, in principle can calculate the mass of the lens. In the case of quasar microlensing, the lens mass is a degenerate value of the relative speed of the quasar and the lens.

An approximate value of the lens mass is given by the equation:

$$Mass = \left(\frac{time \times velocity}{R_{\rm E}}\right)^2 [M_\odot] \tag{63}$$

where the Einstein radius ($R_{\rm E}$) is:

$$R_{\rm E} = \left(\frac{4GM}{c^2}\frac{D_{\rm LS}D_{\rm S}}{D_{\rm L}}\right)^{1/2} [m] \tag{64}$$

where $D_{\rm LS}$ is the lens – source distance and $D_{\rm S}$ is the source–observer distance, $D_{\rm L}$ is the lens–observer distance.

In order to calculate the mass one needs to know the relative velocity. The relative velocity $\upsilon_{\rm T}$ of the lensed system is a composite of three velocities, the transverse velocity of the observer υ_0, the lens velocity υ_l and the source velocity υ_s (Kochanek 2004). The relation between velocities is given by:

$$\upsilon_{\rm T} = \frac{\upsilon_0}{1+z_l}\frac{D_{\rm LS}}{D_{\rm OL}} - \frac{\upsilon_l}{1+z_l}\frac{D_{\rm OS}}{D_{\rm L}} + \frac{\upsilon_s}{1+z_s}. \tag{65}$$

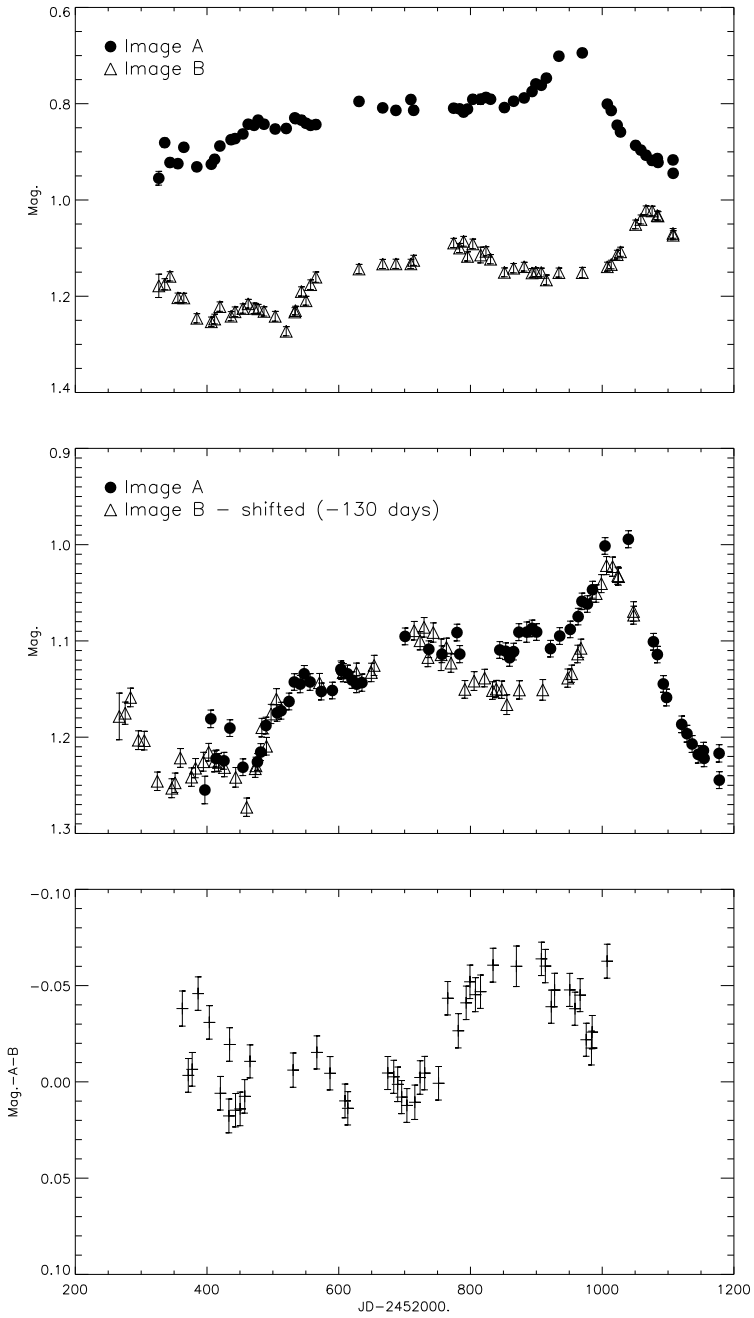

Figure 15: R-band light curves of SBS 1520+530. **Top:** Original light curves of the two images A and B. **Middle:** Time-delay light curves, with the B image offset by −0.69 mag and −130 days. **Bottom:** Difference between linearly interpolated B image and A image.

where: υ_0 is given by equation:

$$\upsilon_0 = \upsilon_{\rm CMB} - (\upsilon_{\rm CMB} \cdot \hat{z})\hat{z} \tag{66}$$

The transverse velocity of an observer can be calculated directly from the galactic coordinates of the source (l,b). A source transverse velocity (υ_s) can in principle be neglected because of the distance ratio. The last factor, υ_l, the lens transverse velocity, can not be calculated directly from observations, because it depends on the local values of κ and γ given for different models. These values are essential for the correct interpretation of microlensing events.

There are different methods for breaking mass – velocity degeneracy, the most popular is ray shooting (Wambsganss 2000). It is based on solving the lens equation, which contains a prior lens model with given κ and γ values.

Since first microlensing detection, research has provided lots of new information about both quasars and galaxies. In most gravitational lensing monitoring programs microlensing events were detected, although its existence can not always be proved due to poor sampling or low signal.

The discovered microlensing events are mostly much weaker than one can expect from simple analysis. Assuming that the mass distribution in the foreground galaxies is similar to the distribution of mass in our Galaxy, (most of the mass is gathered in stars with mass interval 0.001-1) the time scale of microlensing events should be 3 or 4 times longer than those detected. From simple analysis where we assume a point-source and a spherically symmetric lens model, the short length of the microlensing event indicates that in the foreground galaxies most of mass is gathered in Jupiter-like objects or smaller (see GIl-Merino & Lewis).

On the other hand, if the analysis is based on the ray shooting, the same sets of data can be interpreted differently. Now the source is no more lensed on single compact object but, because of the big optical depth, is lensed by many objects at the same time (see Fig 16). In this interpretation the most common compact objects in lensing galaxies are stars in the range of 0.001-1 solar masses.

3.4 Microlensing in spectra

Microlensing has an interesting, observable effect on quasar spectra. Theoretically lensing is an achromatic phenomenon, the deflection angle does not depend on the wavelenght as long as the wavelenght is much shorter than the gravitational radius of the lensing object (Ohanian 1983). Even so, there are a number of conditions which will introduce wavelength dependency in the light curves and in the spectral features of an observed event.

The most remarkable spectral microlensing effect is caused by the size–wavelenght dependency of the source (Schneider 1986). Physical sources, like quasars, have different

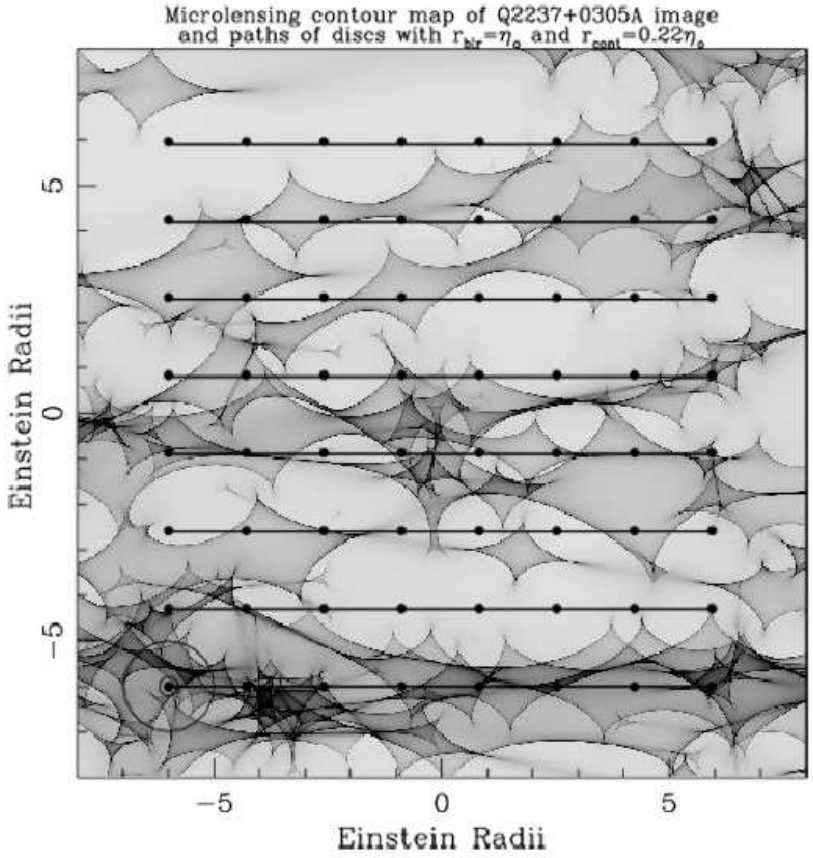

Figure 16: The Figure presents a magnification map. The big circle represents the projected Broad Emission Lines (BLR), the small circle represents the projected continuum region, (Abajas et al. 2005).

apparent size in different wavelength (see Figure 11) and as we know from Section (2.6) only the region close to the caustic is highly magnified and consequently smaller sources are more magnified.

One of the examples is a quasar accretion disk. It is chromatically magnified by microlensing since its apparent size changes with wavelength. Conversely, differences in the maximum magnification constrain the size of the quasar at the observed wavelengths, which can test the accretion disk model for quasars. So called High Magnification Events (HME), are best seen in blue, because the size of the emitting regions of quasars are smaller in the blue than in the red. Similarly, the Broad Line Region (BLR) will be affected by microlensing causing slight variations in the shapes of the lines, which has been predicted to be observable. The relative sizes of quasars are known from quasar spectra studies (see Figure 14) and from quasar spectra monitoring (see Figure 12).

Summarizing, microlensing is a result of a combination of physical events occurring in both the lens and the source, in order to obtain a correct interpretation of such an event one has to take into the consideration the substructure of both the lens and the source.

3.5 Extinction – important parameter in microlensing measurement

From previous chapters we have seen that the microlensing is a small but very important effect in science. In order to get reliable results one should consider galactic extinction, which influences the image brightness and the color. This chapter is based on the work of Elíasdóttir et al. (2006)

Let us first consider how the extinction can be measured.

The most common way for measuring extinction curves is compering spectra of the same type stars, which are located at different distance and at different galactic position. Unluckily, this method is basically limited to the Milky Way stars and the nearest galaxies.

It has been shown that the Milky Way extinction curves in the optical and the ultraviolet changes the mean value depending on the direction, (Cardelli et al. 1989).

$$A_\lambda = R_\lambda E(B-V) \tag{67}$$

The mean extinction value of the Milky Way is $R_v = 3.1$ (Cardelli et al. 1989) and it varies form $R_v = 1.8$ (Udalski 2003) in the direction of the galactic bulge to $R_v = 5.6 - 5.8$ (Cardelli et al. 1989)

The images of a lensed quasar can be treated as "standard candles" shining though distant galaxies. The light coming from images of a quasar, cross a lensing galaxy in different parts, thus it is a very efficient method to estimate the relative extinction curve in high redshift galaxies.

The gravitational lensing is mostly achromatic (see Section 3.4), so the wavelength ratio between the images should be only due to extinction effect. In the case where one of the images of the quasar appears far away from the lensing galaxy, the extinction effect influences one light path, one image will be more red than the other. The extinction affects each data point as:

$$m(\lambda) = \hat{m}(\lambda) - A(\lambda) \tag{68}$$

where: $m(\lambda)$ is the measured magnitude , $\hat{m}(\lambda)$ is the intrinsic magnitude.

By compering quasar images one sees that:

$$\Delta m(\lambda) = (\hat{m}^B - \hat{m}_{\mathrm{A}}) + A_{\mathrm{diff}}(\lambda). \tag{69}$$

In order to understand how the extinction affects quasar image brightness one has to know the extinction law for the given galaxy. But, because of a lack of knowledge about high redshift galaxies we do not have prior knowledge on which extinction law to choose. One solution is to try to fit all known extinction laws to the data and then check which fit is the best.

Let us consider three common extinction laws:

1. Empirical Galactic extinction law, parametrized by Cardelli et al. (1989)

$$A(\lambda) = E(B-V)[R_v a(x) + b(x)] = Aa(x) + \frac{1}{R_v} b(x) \tag{70}$$

where:

- R_v is the ratio of total to selective extinction in the V band, i.e. $R_v = A(V)/E(B-V)$, where E(B-V)=A(B)-A(V)
- $a(x)$, $b(x)$ are polynomials
- $x = \lambda^{-1}$

2. Linear extinction law

Linear extinction law is characteristic for the extinction in the Small Magellan Cloud (SMC):

$$A(\lambda) = A(V) \left(\frac{\lambda}{5500\dot{A}} \right)^{-1}. \tag{71}$$

3. Power law

Power law is an extended linear law:

$$A(\lambda) = A(V) \left(\frac{\lambda}{5500\dot{A}} \right)^{-\alpha}. \tag{72}$$

In order to fit the data points to the given extinction law one should follow the procedure:

- Shift the wavelength of the measured band to the rest frame of the lensing galaxy:

$$\lambda_{\mathrm{j}} = \frac{\lambda_j^0}{(1+z_l)} \tag{73}$$

were: λ_j^0 is the observed wavelength in j band and z_l is redshift of the lensing galaxy

- calculate the magnitude difference in each measured band
- fit the function by substituting $A_{\text{diff}}(V)$ with $A(V)$ in equation 69 where $A(\lambda)$ is one of the three extinction laws described by equation 70, 71, 72.

Additionally, we should keep in mind that the spectra are also affected by microlensing (see Section 3.4), because of different apparent size of quasars in different wavelenght, microlensing change the spectrum, magnifying this wavelenght in which a quasar is the smallest (see Section 12). In order to make proper correction for the microlensing effect one has to calculate the ratio of the spectral line emission to the total emission in each band.

The extinction now has form:

$$(m^B - m^A)(\lambda_j) = A(\lambda_j) + \Delta\hat{m} + sr_j \tag{74}$$

where:

- s is a microlensing parameter,
- r_j is a measured ratio of spectral line emission to total emission in band j.

Now the only thing left is to check which fit is correct for given data. To do it one must estimate the error of the parameters of the fitted extinction curves. One of the methods for estimating the errors is using Monte Carlo simulation. It is based on the generation of many artificial data points with a Gaussian distribution based on real data, which are then fit to it the extinction laws. That fit is correct if the fitted parameters also follow a Gaussian distribution.

There have been several studies based on this theory, one of them, the survey of 10 gravitationally lensing galaxies by Elíasdóttir et al. (2006). That survey used data of galaxies with redshift z=0.04-1.01 obtained by VLT in optical and near infrared bands. Using quasar images Elíasdóttir et al. (2006) explored the effects of extinction.

It was found that seven out of ten system have detectable extinction along one of the light of sight. The mean differential extinction for all seven galaxies was estimated to by $A(V) = 0.56 \pm 0.04$ and ratio of total to selective extinction $R_v = 2.8 \pm 0.4$ which is consistent with the Milky Way.

4 Observations

In this section I present the observational part of my master thesis. I begin by explaining the difficulties involved in planning lensing observations and how one can overcome them. Then I review my monitoring program at the Nordic Optical Telescope (NOT). At the end I present the image reduction and deconvolution procedures and their implementation in the data. The observational data from the NOT are gathered in the Appendix F.

4.1 Planning observation

The main problem with observations of a gravitationally lensed quasar is lack of knowledge what a time delay is. The time delay measurements require well sampled light curves with accurate photometry over a period of a time substantially longer then the time delay. The time delay is not know arbitrary and one has to made a model of lens and calculate a rough time delay before staring observations. The timescale of a quasar variability is also unknown in advance. The procedure of solving this problems is following:

- start to observe with an arbitrary sampling rate,
- reduce data immediately,
- check if any components varies,
- if yes, step-out the sampling rates,
- observe the variety in both components.

Other difficulty with a gravitationally lensed quasar observations is microlensing by stars in a galaxy (see Section 3). The microlensing can change results of about $0.5-1.0$ magnitudes and it is completely unpredictable. Thus, in order to get a time delay out of lensed quasar monitoring one has to observe it with high rating, so that the events like microlensing can be extracted from a quasar variability in the further analysis. In the next section is presented the monitoring program at the NOT which goal was to obtain both the time delay and the microlensing of the gravitationally lensed quasar.

4.2 Monitoring program at the NOT

The data were gathered from the monitoring program done at the Nordic Optical Telescope (NOT) in the period October-April 2005/2006. The approved pilot phase of the program involved monitoring a selected QSO with the NOT for 15 minutes every night. The project relied on cooperation with all observers.

The observing target was gravitationally lensed system SDSS J0903+502 at $z = 3.6$ (Johnston et al. 2003). This system contains the two quasar images (see Table 3) aligned on the opposite side of the lensing galaxy at the redshift $z = 0.388$ (Johnston et al. 2003) with the separation $2''.1$.

Table 3: The astrometric and the photometric results of the SDSS J0903+502 observations at the NOT.

Object	R.A.	Decl.	r mag
A	09 03 35.132	+50 28 20.21	19.99±0.01
B	09 03 34.877	+50 28 18.75	20.78±0.03
G	09 03 34.925	+50 28 19.53	19.59±0.02

The observation was made by use of the three different cameras available at the NOT, ALFOSC and StanCam. The NOT is a 2.5 meters telescope located at Roque de los Muchachos in La Palma, Spain.

During the period, October-April, were gathered 30 images by ALFOSC and 16 by StanCam. All the images were taken in the R-band. On the Figures 21 and 22 are shown the reduced images of the field taken by ALFOSC and StanCam respectively.

The detectors were chosen in order to obtain as far as possible every day data. We were using ALFOSC (The Andalucia Faint Object Spectrograph and Camera) whenever was mounted and StanCam (Stand-by CCD camera) when the other non-optical camera was used.

4.2.1 ALFOSC

The ALFOSC detector (see Table 4) provides optimal parameters. The field of view of the camera is $7' \times 7'$. The seeing during the ALFOSC observations varied from $0''.4$ to $1''.5$. For the small seeing $0''.4 - -0''.5$ our PSF star and the references stars are overexposed, so the exposure time was split into parts: $2\times300s$

Table 4: Properties of the ALFOSC detector.

Active pixels	2048×2048
Field of view	$7' \times 7'$
Readout noise	3.2 e-/pixel
Conversion factor	0.726 e-/ADU
Nonlinearity	+/- 0.2%
Bias Level	240 ADU

4.2.2 StanCam

The StanCam detector has the field of view much smaller than ALFOSC, 3'×3', and bigger readout noise, 6.5 e^-/pixel, but it brought valuable data. On average, during the StanCam observations the seeing was better, 0.″8. Because of the small sensitivity of the camera we were using continues exposure 600s.

Table 5: Properties of the StanCam detector.

Active pixels	1024x1024
Readout noise	6.5 e^-/pixel
Field of view	3'x 3'
Conversion factor	1.68 e^-/ADU
Bias Level	340 ADU

The bias frames obtained by the StanCam detector have occasional horizontal strips (see Figure 17), with a jump of one to two ADUs, the location and the width (in y-direction) of the strips changes between bias frames.

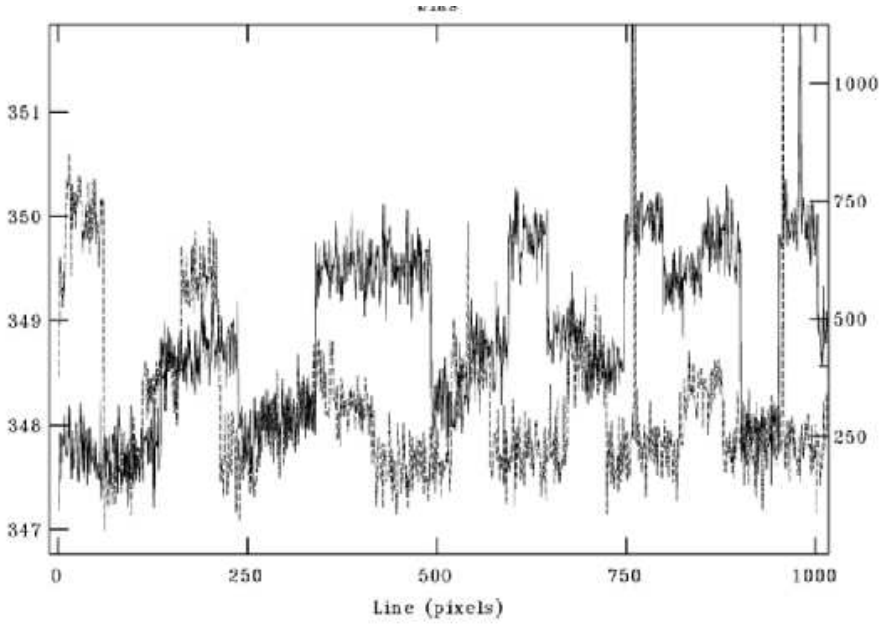

Figure 17: The average of columns 400 to 600 of a StanCam bias frame. The bias frame has occasional horizontal strips (Pursimo 2005).

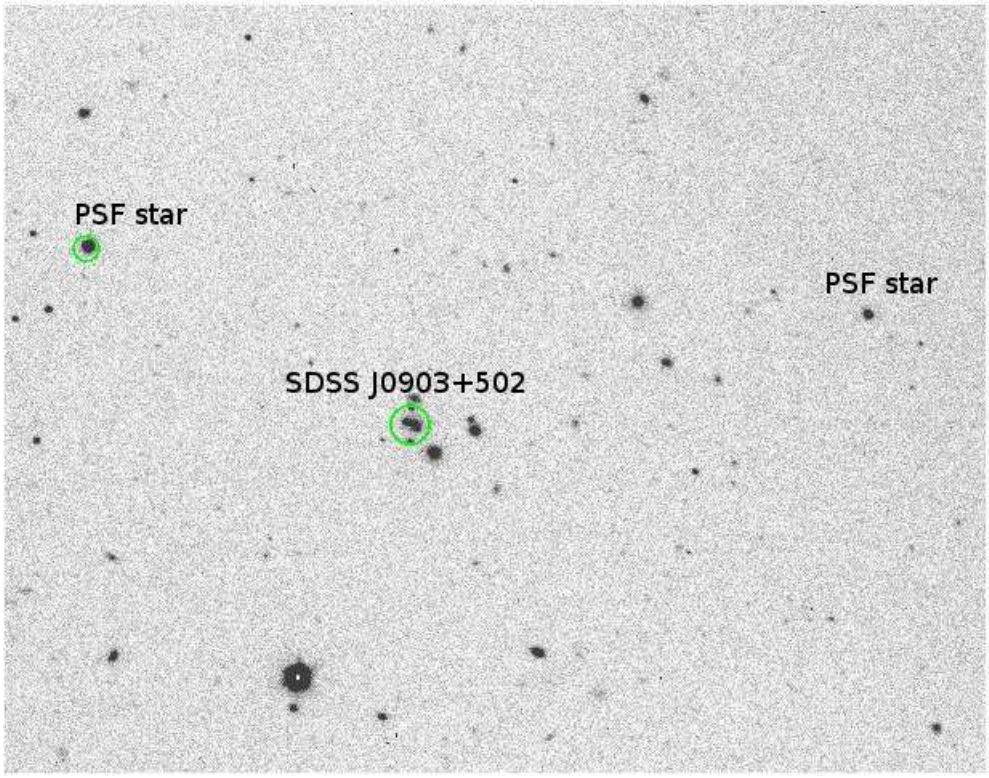

Figure 18: The ALFOSC observations. The image is displayed as the default setup of the ALFOSC camera, the North is up a the West is on the left.

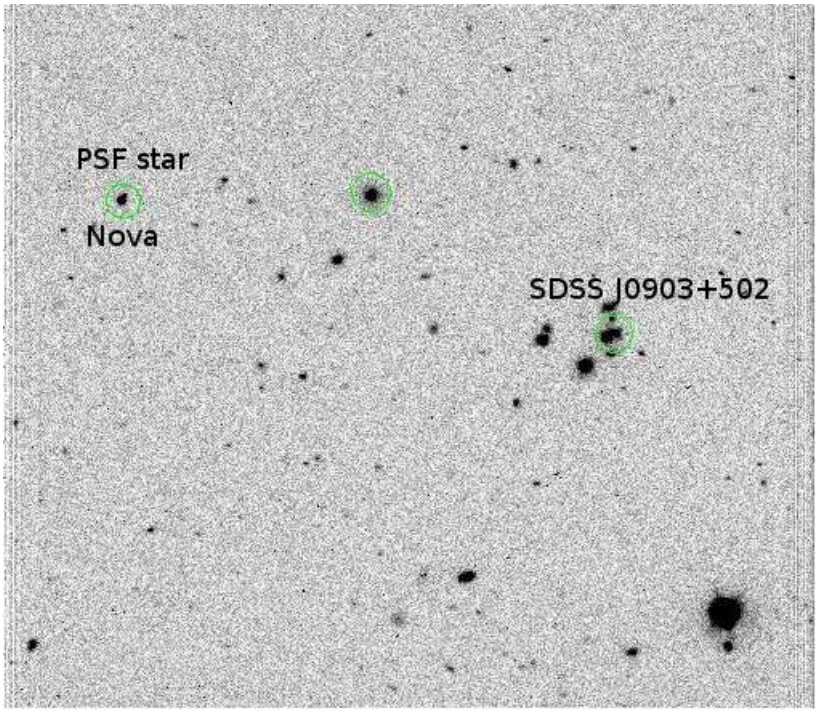

Figure 19: The StanCam observations. The image is displayed as the default of the StanCam camera, the North is up and the West is on the right. The field is flipped in the 'X' axis with respect to the ALFOSC field.

4.3 Aperture Photometry

In order to measure the flux of a star we need to add the intensity of a circular region around the target star (the central aperture), and subtract the estimated background brightness. The background is commonly estimated from values in a annular region surrounding the star.

The larger the aperture we choose, the more of the flux from the star is within the aperture, but the larger the aperture, the larger is the error from the sky subtraction, and the more cosmic ray events will be within the aperture. Thus, the optimal aperture is the one which includes most of the star image (between 3 and 5 times the FWHM of the star)

The most straightforward way to determine the aperture size is to plot flux of star versus aperture size and to choose the minimum aperture for the maximum of the flux.

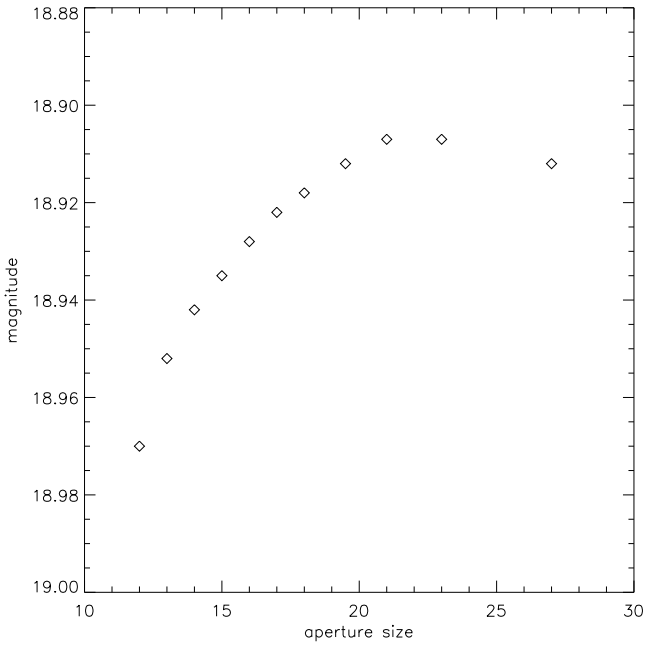

Figure 20: The most straightforward way to determine the aperture size is to plot flux of star versus aperture size and to choose the minimum aperture for the maximum of the flux.

For the purpose of this master thesis, the photometry of all objects were made by use of the IRAF package DAOPHOT.

4.4 Error estimation

Magnitude errors for all objects in this thesis were calculated from the equation:

$$\sigma \simeq 2.5 \log(1 + (S/N)^{-1}) \tag{75}$$

where S/N – is the signal to noise parameter.

One can estimate the expected signal of an object per unit time, at a given telescope and a filter , as well as a statistical noise contribution from an object brightness, a sky background, a dark current and detector read out noise. This calculation makes two assumptions:

- All noise is either independent from the signal (detector read out noise) or is the Poisson noise of the total collected signal in electrons.
- All noise sources are statistically independent from each other and can be added in quadrature.

$$S/N = \frac{S_t}{\sqrt{S_k n T + S_t T + N_d n T + R_d^2 n}} \tag{76}$$

where:

- S_t – is a signal level from a star, integrated over an aperture of n pixels, per unit time,
- S_k – is a signal level from the sky, per pixel, per unit time,
- R_d – is read out noise per pixel in rms electrons,
- N_d – is dark current per pixel per unit time,
- n – is a number of pixels in detection aperture,
- T – is an integration time.

The signal to noise ratio can be also calculated from the S/N ration calculator available at the NOT web page *http://www.not.iac.es/observing/forms/signal/*

If we want to estimate error of the magnitudes on deconvolved images we have to include the error of PSF stars:

$$\sigma_{\rm tot}^2 = \sigma_m^2 + \sigma_{\rm PSF}^2. \tag{77}$$

4.5 Image reduction

The images obtained by a CCD camera are composite of a pure image and signal created by negative effects. Before obtaining the final image, one has to reduce all negative effects which influence the image quality. This negative effects are due to the imperfectness of optics and devices.

The procedure to reduce the effects from the image is to subtract the effects in the opposite direction then the order they interfere with a light beam. Here is shown a brief description what is happening with photons that are coming from the sky to a detector.

- the light is coming into the telescope mirror creating the signal S proportional to the luminosity R_o and the exposure time t: $S = R_o t$,
- the optic system has different degree of vignetting, which reduce the intensity of the light beams coming outside the optics axis, V,
- the dust particles on the filters and the mirrors, also reduce the signal, because they are outside of the focus, their shadows on CCD have shapes of diffraction circles, s,
- the shutter of the detector moves with the finite speed which cause not equal illumination of the detector surface,
- pixels which register coming photons can have different sensitivity, total registered signal depends on the quantum efficiency,
- during the exposure, the detector creates internal charge, this charge is called dark current S_d and it depends on the dark current coefficient, R_d, and the exposure time,
- the detection of light by the CCD camera requires existence of some constant positive electrical charge, B, called offset, because it does not depend on exposure time one can eliminate it by subtracting the image with the zero time exposure frame.

The total signal register by a CCD pixel is given by the equation:

$$S = R_o t V sq + R_d t D + B \tag{78}$$

where $R_o t$ is original signal.

Now we should eliminate the effects in the opposite order. First offset, then dark current and at the end skyflats. The CCD detectors that are cryogenically cooled

(usually to liquid nitrogen temperature – 77 K) do not have dark current. Thus, data from a cryogenically cooled CCD camera need only be corrected by bias and flat field frames. The CCD detectors which are not in the cryogenic temperatures need to be corrected also for the dark current. Apart from the mentioned effects, there is also noise which is not possible to eliminate:

- photon noise,
- thermal noise,
- readout noise,
- ADU noise.

4.5.1 Bias

Bias is the positive charge in the CCD detector, its role is to collect coming photons. It is present on all images.

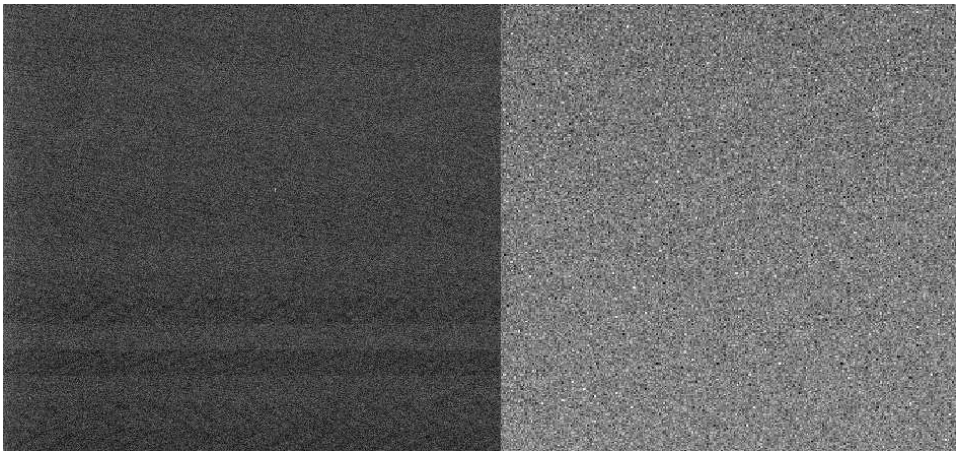

Figure 21: Here we see the two bias frames. Bias is positive charge in a CCD detector, one can obtains it by making a zero exposure image. **Left Figure** shows a single bias frame. **Right Figure** shows combined 3 bias frames which is so called master bias frame. We can see that on the master bias frame all structures which are present on single bias are reduced. It is archived by making median of 3 single bias frames.

To reduce an image from the bias, we subtract a zero exposure image from a science image. Any time we add, subtract, multiply, or divide two images, we are adding the noise to the science image. To reduce the amount of noise in a science image, one should take many calibration images and combine them into a single calibration frame.

Because of the statistic reasons it is good to take an odd number of bias frames, at least three or more and then combine them into a single master calibration image.

When combining calibration frames one should make a median of each pixel. The advantage of median is that when one image has a very discrepant value (i.e. from a cosmic ray) this does not dramatically affect the resultant value (a median is more resistant to one discrepant value than an average). When we take at least three images, it reject almost all cosmic rays.

4.5.2 Flat field

The flat field is a map of a detector sensitivity with a given optics setup. It can be done with taking an image of an equally illuminated surface. There are two possibilities, exposure of the sky during twilight – sky flats, or exposure of an illuminated dome – dome flats. The flat field images also have the bias offset so they need to be corrected by subtracting a bias frame.

Because of stars (in case of the sky flats), or an unequally illuminated dome (in case of the dome flats) one should make few flats and combine them creating median, for better statistic the number of flats should be odd. On Figure 25 are represented, the single sky flat field image (left) and the master sky flat field image (right). On left Figure there are few faint stars on the right Figure they are reduced.

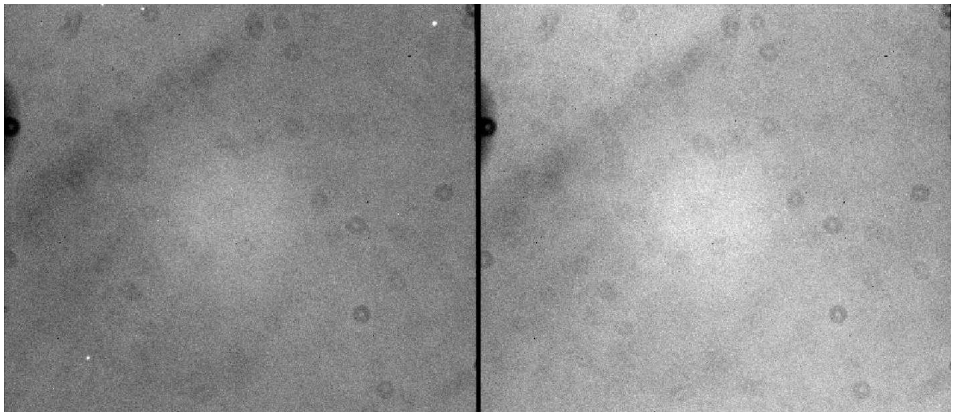

Figure 22: On the Figure are presented the two flat field frames. The flat field is a map of a detector sensitivity with a given optics setup. It can be done with taking an image of an equally illuminated surface. **Left Figure** shows a single flat field frame. **Right Figure** shows combined 3 flat field frames in so called master flat field frame. We can see that on the master flat field frame all stars which appear at single flat field are reduced. It is archived by making median of 3 single flat field frames.

The flat field image has a large number of counts per pixel, whereas our science images have relatively few counts per pixel. If we simply divide one by the other,

all the pixels in the resultant image would have very small values. We should only slightly modify the counts in the science frame enough to correct the multiplicative errors without significantly changing the pixel values in the science image. One can do this dividing the flat field image by a constant, which makes the pixels value in the flat field frame close to one.

4.5.3 Applied Reduction

All data used in this thesis were manually reduced by use of the standard IRAF packages. The reduction of all frames were following theory explained in chapter 4.5. The images were bias and flat field reduced. The cameras used for observations were liquid nitrogen cooled, thus no dark frame were needed.

For combining the bias and the flat frames was used the IRAF commands from the CCDRED package *combine* with median as a parameter. For extraction was used the IRAF command from the IMGTOOLS package *imcalc*.

4.6 Deconvolution

The Hubble constant estimation from gravitational lensing requires high resolution imaging. One of the mathematical methods to obtain it, is deconvolution. Deconvolution is the method which helps to recover and separate signal from sources. Deconvolution, simply saying, is a mathematical method for improving the resolution of astronomical images.

4.6.1 Theoretical description

Astronomical images are obtained by finite size telescope and finite pixel size CCD cameras, so in principle all observed point objects have its finite size images.

A finite image size of the point source seen through a telescope has two basic origin. First, a point source seen through a telescope has an angular size inversely proportional to a diameter of a primary mirror, thus, since a telescope does not have an infinitely large mirror it wont give a point image. Second, if a telescope is ground based an image is additionally blurred by turbulent motion in the Earth's atmosphere. There are two ways for improving the resolution of an image. One is technical (adaptive optics, out space telescope) other is numerical - the image processing (Magain 1998). Since I did not have influence on the technical part of observations, we will focus on the image processing.

Mathematically speaking the observed image is a convolution of the real light distribution with so called "total blurring function" or "point spread function (PSF)". So

the image equation has form:

$$d(x) = t(x) * f(x) + n(x) \tag{79}$$

where:

- $d(x)$ – an observed light distribution,
- $f(x)$ – an original light distribution,
- $t(x)$ – a total point spread function (PSF),
- $n(x)$ – a measured error affecting data.

As I mention on the beginning of this section the finite pixel size of a CCD camera also has influence on an image. In the mathematical point of view it causes that the functions $f(x), d(x), t(x), n(x)$ have discreet values:

$$d_i = \sum_{j=1}^{N} t_{\mathrm{ij}} f_j + n_i \tag{80}$$

where N is number of pixels on a CCD camera.

The goal of the deconvolution is having an image, d_i (sampled vector of d(x) function) and a PSF, t_{ij} (sampled vector of t(x) function), obtain an original light curve f_j.

The deconvolution is an inverse problem which additional with noise is a problem without one unique solution. The method for choosing the one interesting solution is the minimizing method. This method is simply based on the difference minimum between the data and mathematical model:

$$S_1 = \sum_{i=1}^{N} \frac{1}{\sigma_i^2} (\sum_{j=1}^{N} t_{\mathrm{ij}} f_j - d_i)^2 + \Lambda H(f_1, ..., f_N) \tag{81}$$

where:

- $\frac{1}{\sigma_i^2}(\sum_{j=1}^{N} t_{\mathrm{ij}} f_j - d_i)^2$ – is the the χ^2 with the standard deviation (σ_i) of the image intensity at i-th point,
- H – is a smoothing function,
- Λ – is a Lagrange parameter, which is determined so that model is statistically compatible with the data.

This method can be improved by putting the restriction on the result, for example the positivity of the signal, so that solutions with negative intensities can be rejected.

The described general deconvolution theory can have few realization, most of them suffer two basic problems:

- they produce artifacts in the vicinity of the objects,
- the ratio of the stars intensities is not constant.

The two problems are caused by a violation of the sampling theorem. One of the solutions for that problems is to, instead of using function t(x) in equation 79, use a narrower function s(x), so that a deconvolved image has its own PSF, r(x). The functions are related as following:

$$t(x) = r(x) * s(x). \tag{82}$$

Function s(x) ensures that the sampling theorem is not violated and additionally an image shape of a point source is precisely known, it is r(x). Now the original light distribution we can written as:

$$f(x) = h(x) + \sum_{k=1}^{M} a_k r(x - c + k) \tag{83}$$

where:

- M – is a number of point sources,
- a_k – are intensities of point sources,
- c_k – are coordinates of point sources,
- h(x) – is an extended component (background).

To the deconvolution algorithms often is added smoothing function given by equation:

$$H(f_1, ..., f_N) = \sum_{i=k}^{N} \lambda_i (h_i - \sum j = 1^N r_{ij} h_j)^2. \tag{84}$$

It cause that the calculated residuals are statistically distributed with the correct standard deviation in any subpart of the image. The normalized residual images (observed data minus convolved model, divided by σ) are smoothed with an function, so that values of pixels are replaced by a weighted mean value of its on vicinity. The λ is adjusted for the residuals to be close to 1 everywhere.

4.6.2 Deconvolution of SDSS J0903+502

All images obtained at the NOT in period September-April 2005/2006 of the lensed quasar system SDSS J0903+502 was deconvolved by use of the "PSF Controled Deconvolution" software created by Magain (1998). The analysis used in the software is based on theory explained in previous section. Here is shown how deconvolution was applied to the SDSS J0903+502 field.

4.6.3 Field

SDSS J0903+502 is a field where most of the objects are high redshift galaxies. Figure 26 shows an image of the SDSS J903+502 field taken by StanCam, with marked galaxy/star types of the objects where × is a galaxy and ◯ is a star (the full information about objects in the field contains Appendix G). On the Figure 26 we see only six stars where one of them is with close by companion, one of them is overexposed and three of them are faint. In the next section it is explained why lack of single bright stars is a problem.

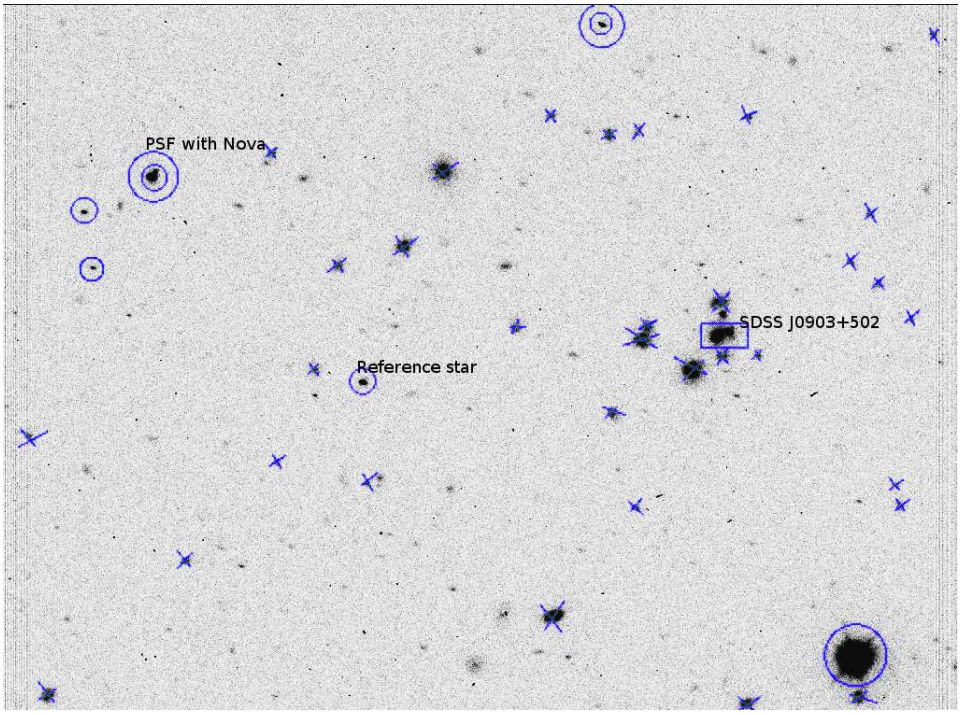

Figure 23: Here is presented an image of the SDSS J0903+502 field taken by StanCam. The ×, ◯ and □ symbols present galaxies, stars and quasar images respectively. Double ◯ marks the stars with close by companion.

4.6.4 PSF-stars

Point Spread Function (PSF) plays essential role in the deconvolution process, thus it is important to choose the correct object as a PSF star. The PSF has to satisfies the following criteria:

- it has to by a star,
- it can not have any close neighbors,
- it should not be far away from the object for deconvolution,
- it should be about as bright as the object we want to deconvolved.

As we know from Chapter 4.6.3 the SDSS J093+502 field contains mainly galaxies, there are basically only two stars on the field which satisfy all PSF-star requirements (see Table 6).

PSF–star of ALFOSC	
SDSS name	SDSS J090343.12+502900.9
RAJ2000	09 03 43.12
DEJ2000	+50 29 01.0
class	6
rmag [mag]	17.847
error rmag [mag]	0.006
PSF–star of ALFOSC and StanCam	
SDSS name	090323.74+502846.9
RAJ2000	09 03 23.74
DEJ2000	+50 28 47.0
class	6
rmag [mag]	19.497
error rmag [mag]	0.017

Table 6: Physical parameters of the stars used as PSF–stars in ALFOSC and StanCam observations.

Both of them, were used for deconvolution of quasar on ALFOSC images. Because of the small field of StanCam camera there is only one of the PSF star.

On average a star, J090323.74+502846.9 was giving better deconvolution results and that one was chosen to be a PSF–star on all StanCam images.

Reference star 1 for ALFOSC	
SDSS name	J090344.07+502845.9
RAJ2000	09 03 44.08
DEJ2000	+50 28 45.9
class	6
rmag [mag]	20.189
error rmag [mag]	0.025
Reference star 2 for ALFOSC	
SDSS name	J090344.90+502843.5
RAJ2000	09 03 44.90
DEJ2000	+50 28 43.6
class	6
rmag [mag]	21.046
error rmag [mag]	0.049
Reference star for StanCam	
SDSS name	J090327.99+502809.2
RAJ2000	09 03 27.99
DEJ2000	+50 28 09.2
class	6
rmag [mag]	21.200
error rmag [mag]	0.056

Table 7: Physical parameters of the stars used as reference in ALFOSC and StanCam observations.

4.6.5 Residuals

Residuals are created from subtraction of the original image from the model. They are visualizing correctness of the deconvolution program, thus, smaller residuals means better deconvolution. In practice the resultant residual image should be flat and on average equal 1.

On the Figure 24 are shown the examples of the residuals. The deconvolution creates better or worst models depending of many effects which theory was described in Section 4.6.1.

The deconvolution algorithm creates better models when the difference between output point spread function and the input point spread function is bigger, thus to more blurred images it is easier to adjust the model. One can easily see this effect on Figure 24. The right Figure shows the high resolution image with not perfectly flat residual image and the left Figure shows blurred image with nearly perfect flat residual image.

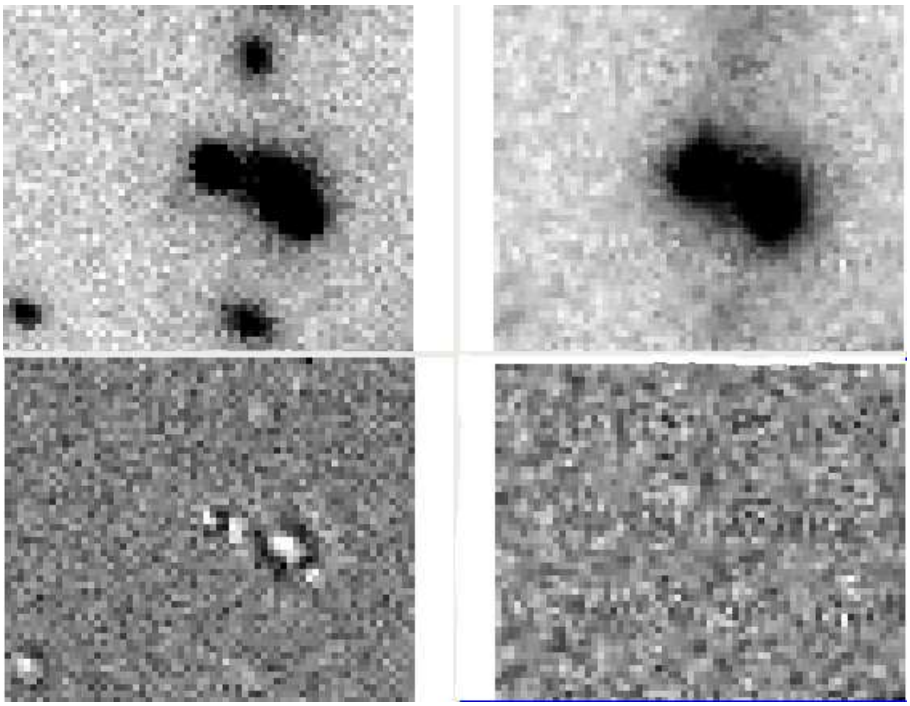

Figure 24: *Top*: Images of the quasar made during good and bad atmospheric conditions left – 1.″2, right–0.″8. *Bottom*: Residuals corresponding to the quasar images at the top of the Figure, left image shows flat residuals corresponding to the bad atmospheric condition, right image shows not flat residual corresponding to the good atmospheric conditions

Apart from the model finding problem for the high resolution images, there are some situations where none of the models considered by program fits to original image, one of this situations is when the objects for deconvolution are elongated.

From Chapter 4.6.1 we know that deconvolution algorithm extracts point-spread function (PSF) from PSF-star and adjusts it to the mathematical model of an object. In order to fit the PSF and the model correctly and obtain a flat residual image, the object has to be a point or has to be composed of few point objects. Thus, program will not deconvolve properly any elongated objects.

Before starting the deconvolution process one need to make sure that the objects for deconvolution are points. The elongation of point objects might have happen mainly due to technical reason. The optics of telescope can have astigmatism or simply can be out of focus, in both cases a point object will have elongated shape and deconvolution will not work. The situation with not well focused telescope is shown at the Figure 25. Left Figure shows image of lensed system trough defocused telescope, the right Figure shows residuals with lots of peaks much above 1.

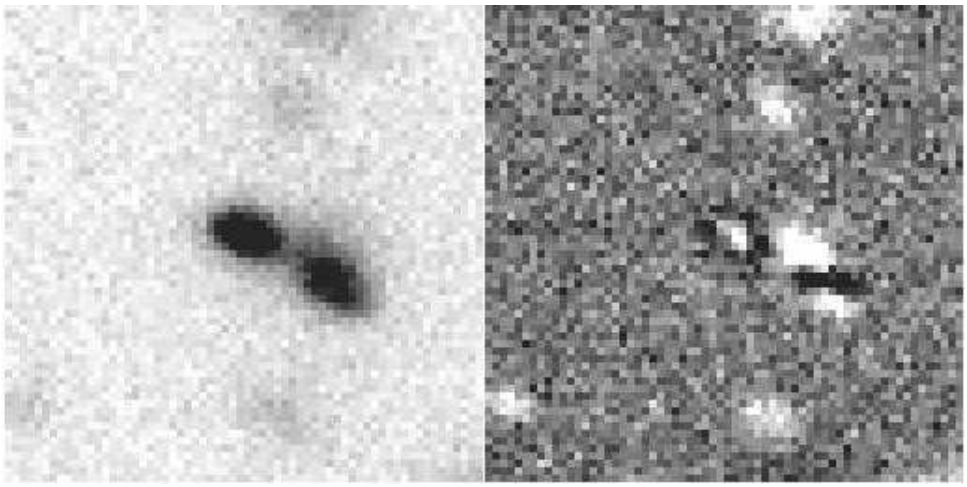

Figure 25: When the telescope is out of focus, point objects are elongated and deconvolution does not work properly. **Left Figure** shows image of lensed system trough defocused telescope. **Right Figure** shows residuals with lots of peaks much above 1.

For the final test for correctness of the deconvolution are used smoothed and squared residuals:

- the residual images can not have bumps well above 1 in the place where object for deconvolution is,
- if there is a bump more the 4 counts on residual images then the data point should be rejected.

In Chapters 4.4.3 and 4.4.4 was presented that the field around the quasar SDSS J0903+502 has very few stars. On the ALFOSC images there are only two good objects for PSF and on the StanCam images only one, this caused that we had no choice with PSF and reference stars, thus deconvolution did not succeed on all frames. We have lost 9 data point from ALFOSC observation after deconvolution due to two main reasons:

- overexposed PSF star – 3 frames
- not well focused telescope (elongated objects) – 9 images

5 Results

This section presents the results of a half year of observations done at the Nordic Optical Telescope in the period October 2005 – April 2006. Here I present the analysis and conclusion from reduced and deconvolved images. At the beginning of this Chapter it is shown how the deconvolved images look and the astrometric and photometric results are presented. Next, I introduce the techniques and results of the SDSS J0903+502 lens modeling. At the end I present the light curve of the quasar images and its analysis.

5.1 Deconvolution results

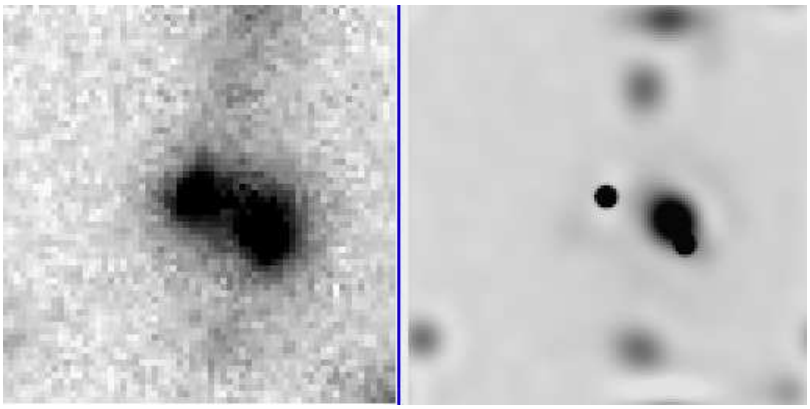

Figure 26: Image from ALFOSC and its deconvolved model.

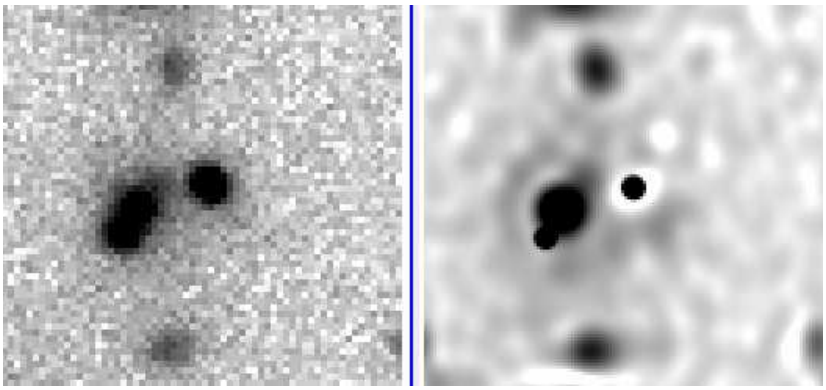

Figure 27: Image from StanCam and its deconvolved model.

Deconvolution of the gathered images from ALFOSC and StanCam observations went mostly successfully (see Chapter 4.6.2). Here are presented results of the correctly

deconvolved images.

On the Figures 26 and 27 are presented images from ALFOSC and StanCam observations respectively and their deconvolved models and on the Figure 28 is presented the deconvolved image in details. On the first frame from the Figure 28 we can see modeled by the deconvolution algorithm background containing the lensing galaxy, on the second frame there are the images of the quasar and the last frame shows the combination of the two previous frames, it is the deconvolved image of the SDSS J0903+502 lensed system.

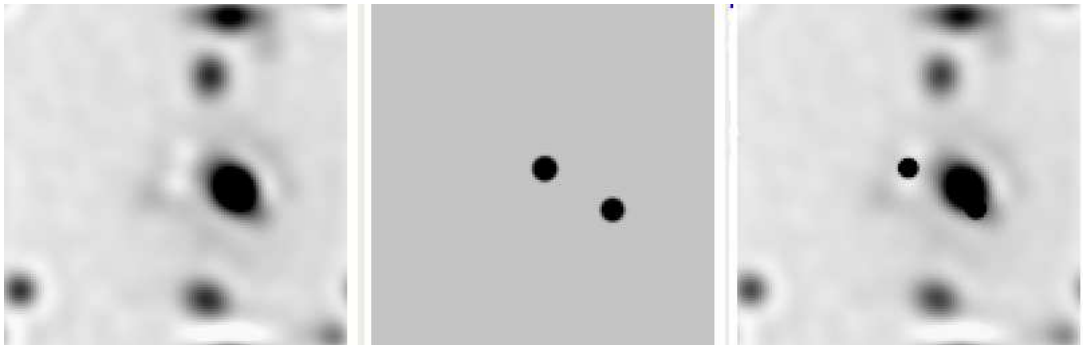

Figure 28: From left to right we can see modeled by the deconvolution algorithm background containing the lensing galaxy, then the images of the quasar and the last frame shows the combination of the two previous frames, it is the deconvolved image of the SDSS J0903+502 lensed system

From that images we have measured positions and magnitudes of the both quasar images and the lensing galaxy (the astrometric and the photometric results are gathered in the Tables 8 and 9.

Objects	Separation
A–B	2.″8
A–Galaxy	2.″0
B–Galaxy	0.″8

Table 8: Astrometric and photometric results

5.2 Lens modeling

In this section it is described the modeling of the gravitationally lensed system SDSS J0903+502 by use of the GRAVLENS software created by Chuck Keeton for the CASTLES project. The modeling is divided in two parts. In the first one we assume that lens is a point

Object	R.A.[hh:mm:ss]	Decl.	r mag
A	09 03 35.132	+50 28 20.21	20.219±0.05
B	09 03 34.877	+50 28 18.75	20.97±0.05
G	09 03 34.925	+50 28 19.53	19.51±0.05

Table 9: Astrometric and photometric results

in order to calculate the Einstein radius and an approximate mass on the lens. In the second we assume that lens is Singular Isothermal Sphere (SIS) and we calculate the transverse velocity.

From both models we are also estimating the theoretical time delay of the system, which will be used in the next sections.

5.2.1 Einstein radius

In the previous sections we have calculated that the two images of the quasar are separated by $2\farcs8$. This separation gives us the lower limit on the Einstein radius (see Chapter 2.2). From the quasar images condition we know that:

$$\Delta\theta \geq \theta_e. \tag{85}$$

This value gives also a constrain upon the mass of the lens. We can calculate an approximate lens mass using the definition of the Einstein radius from the Chapter 2.2:

$$\theta_e = \sqrt{\frac{D_{\mathrm{LS}}}{D_{\mathrm{OS}} D_{\mathrm{OL}}} 4MG}. \tag{86}$$

Using equation for the cosmological angular distance we calculate $D_{\mathrm{LS}}, D_{\mathrm{OS}}, D_{\mathrm{OL}}$. Assuming the flat Universe with $\Omega_m = 0.3$, $\Omega_\Lambda = 0.7$ and $H_0 = 70$ (see Table 10) we get:

- the observer-lens distance is $D_{\mathrm{OL}} = 1.66$ Gpc,
- the observer-source distance is $D_{\mathrm{OS}} = 15.42$ Gpc,
- the lens-source distance is $D_{\mathrm{LS}} = 13.76$ Gpc.

Putting the calculated distances to the equation 85 and 86 we get the upper limits of the Einstein radius and the mass for the SDSS J0903+502 lensing galaxy:

- $\theta_e \leq 1\farcs4$
- $Mass \leq 9.5 \times 10^{12} M_\odot$

Hubble constant	Quasar z=3.6	Galaxy z=0.388
50	21.59	2.33
60	17.99	1.94
70	15.42	1.66

Table 10: Distances to the galaxy and the quasar for the different Hubble constant calculated for the flat Universe.

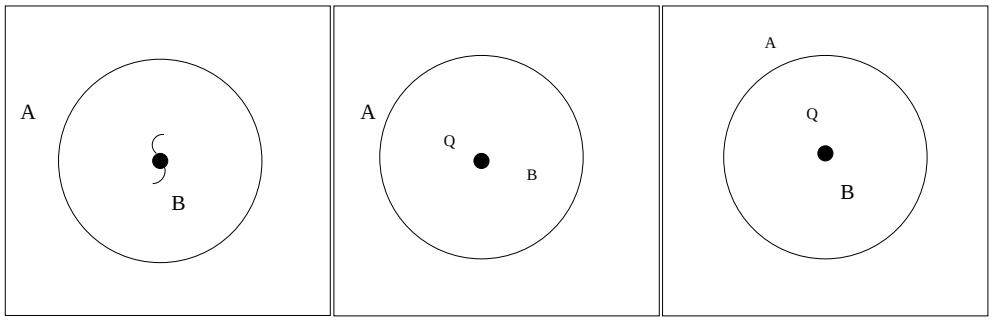

Figure 29: The solution of the point-like lens model has only symmetrically aligned quasar images. Our system is not symmetrical. The images of the quasar and the galaxy does not lie at the same line, thus the point-like lens model does not give us the correct solution. From the modeled quasar position we get or the proper position of A image and the wrong position of B image or opposite.

Assuming simple point-like lens model we can try to find the approximate quasar position. Using the known positions of the quasar and the galaxy (see Table 11) we can easily calculate the modeled positions and magnifications of the quasar images from the equations:

$$\theta_1 = \frac{1}{2}(\beta + \sqrt{\beta^2 - 4\theta_e^2}) \tag{87}$$

$$\theta_2 = \frac{1}{2}(\beta - \sqrt{\beta^2 - 4\theta_e^2}) \tag{88}$$

$$\mu_1 = \left(1 - \left[\frac{\theta_e}{\theta_{1,2}}\right]^4\right)^{-1} \tag{89}$$

$$\mu_2 = \left(1 + \left[\frac{\theta_e}{\theta_{1,2}}\right]^4\right)^{-1} \tag{90}$$

Under assumption of the point like lens, the quasar should be positioned $1''.1$ from the galaxy. On Figure 5.2.1 is shown the results of point like lens modeling using

Object	x	y	R.A.	Decl.
A	2.″0	0.″7	09 03 35.132	+50 28 20.21
B	-0.″4	-0.″7	09 03 34.877	+50 28 18.75
Galaxy	0.″0	0.″0	09 03 34.925	+50 28 19.53
QSO	1.″25	0.″42	09 03 36.175	+50 28 19.95
	0.″6	1.″4	09 03 35.525	+50 28 20.93

Table 11: The quasar images positions and the modeled position of the quasar from the point-like lens model. The point-like lens model does not give us the correct solution, when we get the proper position of A image we get the wrong position of B image and opposite. The source position is calculated for A and B images separately.

GRAVLENS software. It is shown the size of the modeled Einstein radius and the apparent and the real position of the quasar. A, B and Q represent the apparent position of quasar images and the real position of the quasar. In the center of the plot, at the position x=0 and y=0 is placed the lensing galaxy.

The solution of the point-like lens model has only symmetrically aligned quasar images. Our system is not symmetrical, the images of the quasar and the galaxy does not lie at the same line, thus the point-like lens model does not give us the correct solution. From the modeled quasar position we get or the proper position of A image and the wrong position of B image or opposite (see Table 12 and Figure 29).

5.2.2 Transverse velocity

The next step in modeling is to assume that the lens is an Singular Isothermal Sphere. Here instead of using the Einstein radius, θ_{mE} we will use the deflection angle α. We know that for α there is one constrain $2\Delta\theta \geq \alpha$. In case of the SDSS J0903+502 quasar we have $\alpha \leq 1.''4$. We will use α to calculate positions of the quasar images. The exact deflection angle can be calculated from the equation:

$$\alpha = 4\pi \left(\frac{\sigma}{c}\right)^2 \frac{D_{\mathrm{LS}}}{D_{\mathrm{S}}} \tag{91}$$

where σ is a transverse velocity described by the equation:

$$\alpha = \sigma D_{\mathrm{OS}} D_{\mathrm{OL}} 4\pi. \tag{92}$$

Putting the constrain for the deflection angle into the equation 92 one can find the limitation for the transverse velocity is $\sigma \leq 243$ [km/s].

In order to get the constrains on the lens shape we have to find the approximate ellipticity of the galaxy and its direction. From an analysis of deconvolved images of our object (see Figure 35) we have:

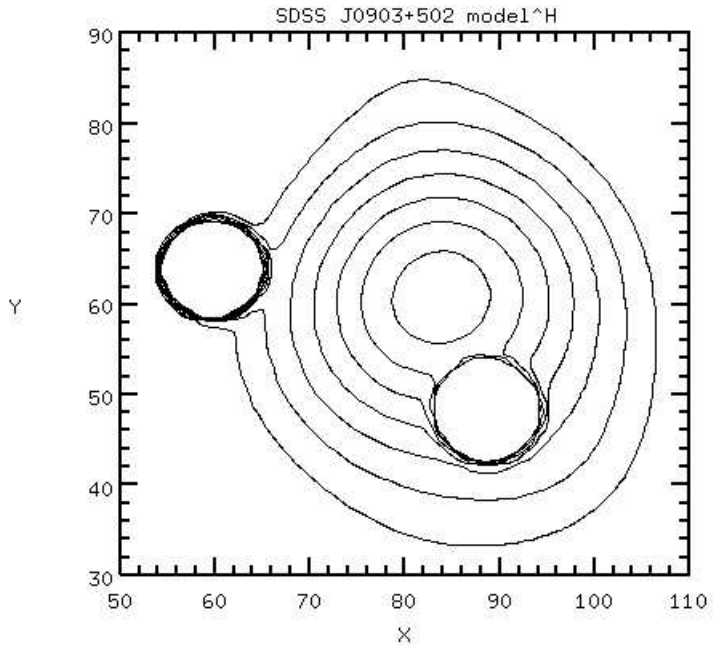

Figure 30: An contour plot of the deconvolved image from the ALFOSC observations.

- $\epsilon = 0.4 \pm 0.1$
- $\theta_\epsilon = 4^\circ \pm 4^\circ$

This values are only estimations, thus those parameters are inserted into lens modeling only as initial parameters.

Name	Value
Image A position	$x_\mathrm{A} = 6\farcs20 \pm 0\farcs005$, $y_\mathrm{A} = 6\farcs33 \pm 0\farcs005$
Image B position	$x_\mathrm{B} = 8\farcs60 \pm 0\farcs005$, $y_\mathrm{B} = 4\farcs88 \pm 0.005$
Images flux	$F_\mathrm{A} = 43.25 \pm 8.6$, $\frac{erg}{scm^2A}$, $F_\mathrm{B} = 20.09 \pm 4.0$ $\frac{erg}{scm^2A}$
Galaxy position	$x_\mathrm{G} = 8\farcs23 \pm 0\farcs5$, $y_\mathrm{G} = 5\farcs60 \pm 0\farcs5$
Galaxy flux	$F_\mathrm{G} = 70.00 \pm 14.00$
Eccentricity	$\epsilon = 0.4$
Eccentricity direction	$\theta_\epsilon = 4^\circ$
Deflection angle	$\alpha = 1\farcs4$

Table 12: Model constrains

In Table 12 are summarized all information from the deconvolved frames about the system. We have used them as constrains in the modeling. The strongest constrains

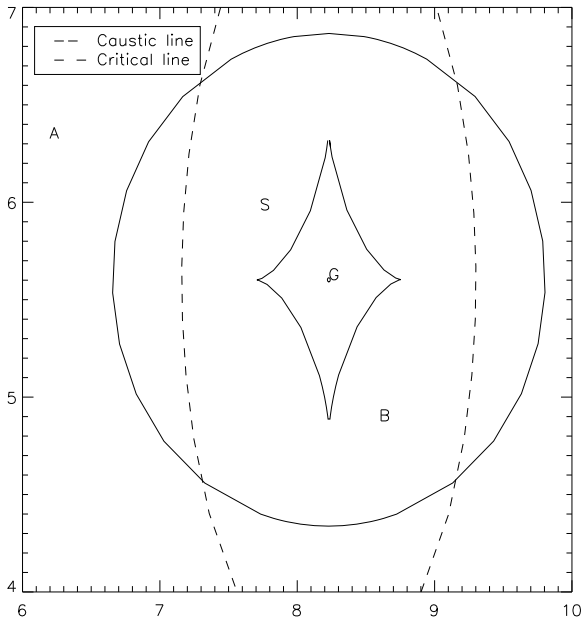

Figure 31: Here are presented the results of modeling. There are shown modeled caustic (solid line) and critical (dashed line) curves with marked positions of source (S), quasar images (A, B) and galaxy (G).

are the quasar images positions. Next two constrains, the images fluxes, are also well known from the deconvolved frames. We put into images fluxes constrain errors of 20% because they vary due to the quasar intrinsic variability and the microlensing.

Last five constrains, the parameters concerning the galaxy and the mass scale (deflection angle) are rough estimations which in this model play role of initial parameters.

The biggest uncertainty with our model is the direction of the ellipticity of the lensing galaxy. Thus, the modeling procedure was first to put all initial parameters as constrains for the model and let them change within the error. Then as a result find the real ellipticity direction of the lens. Having this estimated we run GRAVLENS program putting all the galaxy's constarins and the mass scale as parameters to be modeled (see Table 13).

On the Figure 32 are presented the results of the modeling, there are shown the modeled caustic (solid line) and the critical (dashed line) curves with marked positions of the source (S), the quasar images (A, B) and the galaxy (G). On Figure 33 it is shown the critical and the caustic lines on the background of one of the deconvolved images from the ALFOSC observations.

Using the modeled lens one can also calculate the theoretical time delay of the

Name	Value
Galaxy position	$x_{\rm G} = 8.23\pm$, $y_{\rm G} = 5\farcs60$
Ellipticity	$\epsilon = 0.48$
Ellipticity direction	$\theta_\epsilon = 0\fdg09$
Deflection angle	$\alpha = 1\farcs34$

Table 13: The parameters in the SIS model.

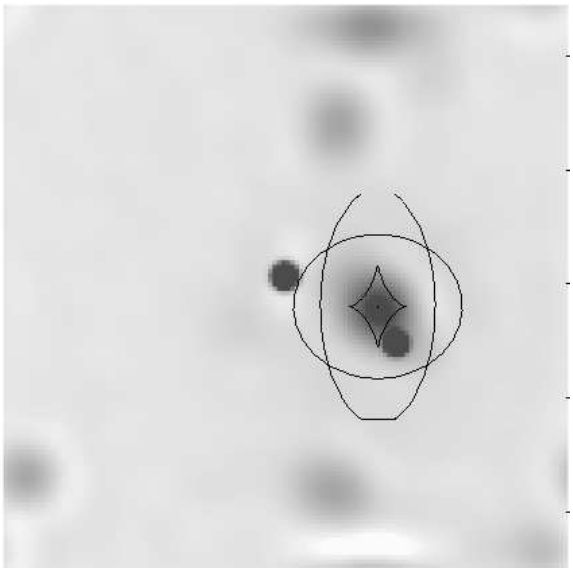

Figure 32: Here are shown the critical and the caustic lines on the background of one of the deconvolved images from ALFOSC observations

system. We use the analytical equation for the time delay for SIS model:

$$\Delta t = \frac{D}{2c}(1+z_l)(r_j^2 - r_i^2) \tag{93}$$

and as an error bar we check how the results changes depending on the added external shear $\gamma = 0.1$

$$t_{\rm min} = \frac{D}{2c}(1+zl)\left((r_j^2 - r_i^2) - \gamma\sqrt{r_j^4 + r_i^4 - 2r_i^2 r_j^2 cos(2\phi)}\right) \tag{94}$$

$$t_{\rm max} = \frac{D}{2c}(1+zl)\left((r_j^2 - r_i^2) + \gamma\sqrt{r_j^4 + r_i^4 - 2r_i^2 r_j^2 cos(2\phi)}\right) \tag{95}$$

The results are gathered in Table 16. We see that the predicted time delay changes significantly depending on the shear.

Analytical equation	mean=45.88 days, max=64.24 days, min=27.53 days

Table 14: Model parameters

5.3 SDSS J9003+502 light curve

On Figure 34 are presented the light curves of the quasar images and the reference star. The light curves were obtained as the results of the deconvolution of ALFOSC and StanCam frames. Because of the problematic deconvolution described, in details in Chapters 4.6 and 5.1, of both data sets from all 46 data points only 29 could be included. The reference star seen at the plot is the comparison star from the ALFOSC observations. After deconvolution we have noticed that for the StanCam observations the reference star is variable.

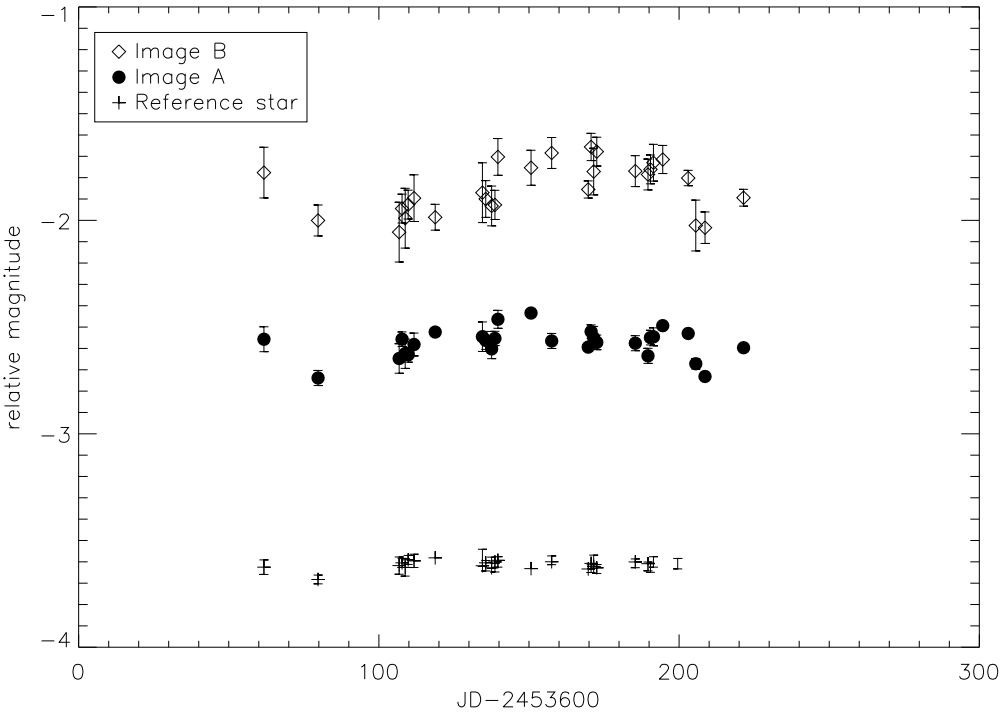

Figure 33: Here are presented light curves of quasar images and reference star. The light curves were obtained as the results of deconvolution of ALFOSC and StanCam frame. Because of problematic deconvolution described in details in Chapters 4.7 and 5.1 of both data sets from all 46 data points only 29 could be included. The reference star seen at the plot is the comparison star for ALFOSC images.

Having the light paths of both quasar images our goal is to estimate the time delay. In order to obtain it we need to estimate the degree to which this the two series are correlated. Here we will apply two methods, by eye and mathematical (cross correlation).

The method by eye is a rough estimation which helps to verify the correctness of the mathematical methods and it is based on looking for any magnifications events in both curves and correlating them.

On the Figure 34 one can see a magnification bump in the A image light curve between 80 and 180 days and in the B image light curve magnification bump is between 110 and 140 days, thus we can roughly estimate that it is 30-50 days. Because of the small variability of the quasar this method does not give clear results when applied for the SDSS J9003+502 light curves.

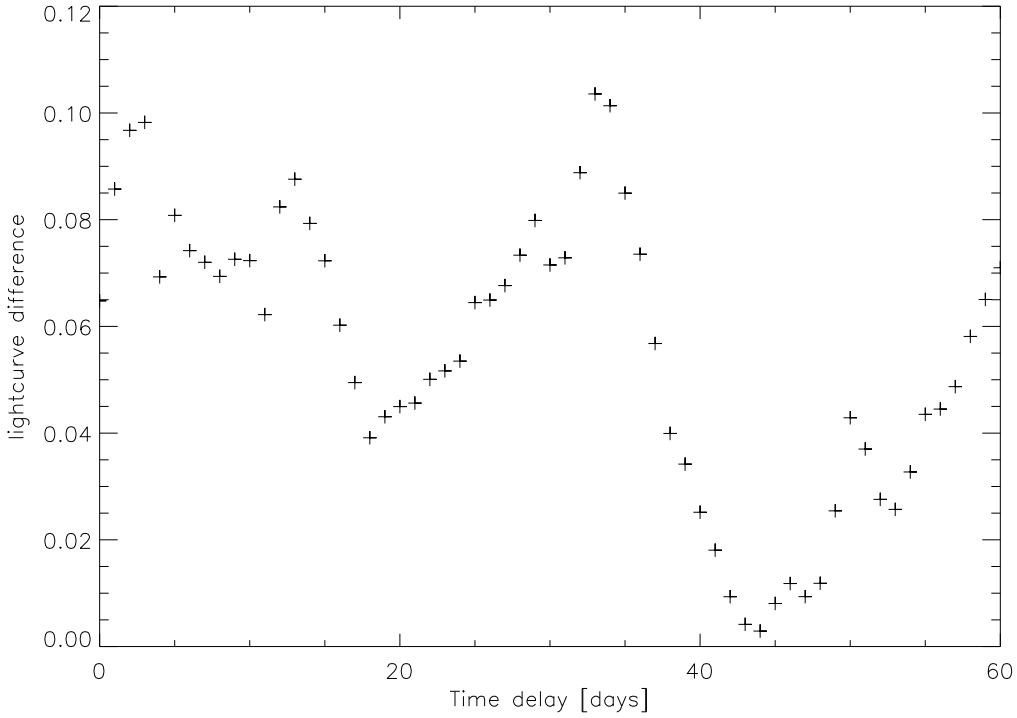

Figure 34: The mathematical method, cross correlation, is based on shifting one data set in time and magnitude, interpolating the shifted data and calculating a light curve difference

The mathematical method, cross correlation, is based on shifting one data set in time and magnitude, interpolating the shifted data and calculating a light curve difference.

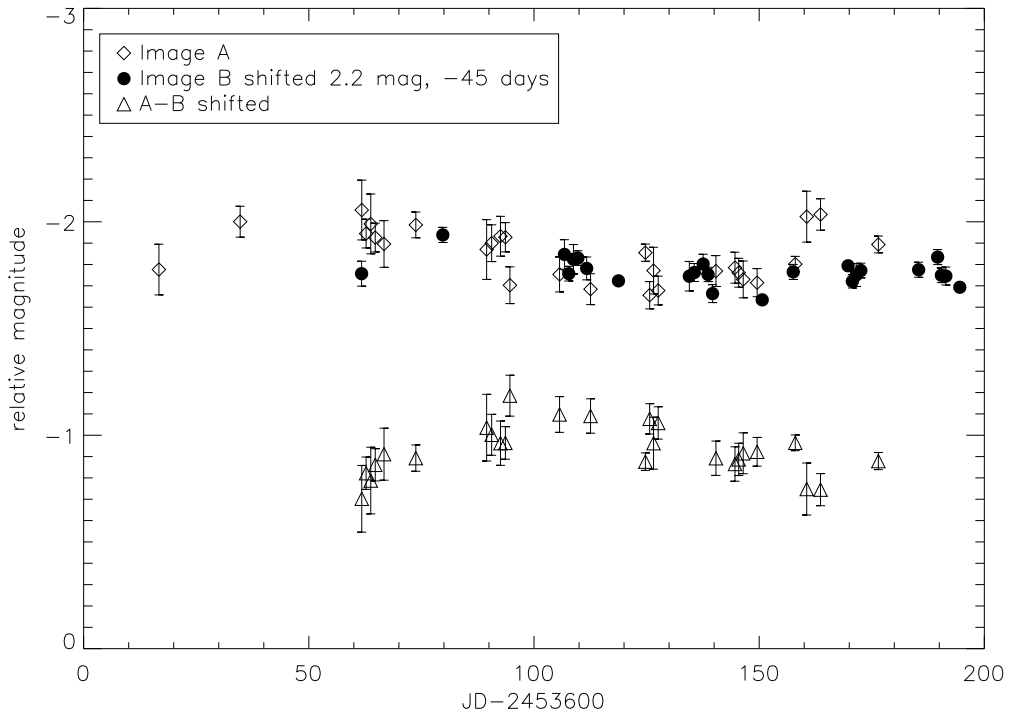

Figure 35: Here is presents the light curves difference. The B quasar image has been shifted in magnitude -0.8 offset and time -37 and we have linearly interpolated it on A image. On top are shown two light paths where B image light path is shifted in time and magnitude. On bottom is light curves difference obtained by use of linear interpolation.

On the Figure 36 are presented the results of the mathematical method applied to the SDSS J9003+502 light curves of A and B images. We have been shifting the B image light path back in time and linearly interpolating the A image data set on the B image data set. We have found that for the magnitude shift 0.8 and the time shift -43 days the cross correlation reaches minimum. We can assume that probable time delay is for the mean light curve difference lower then 0.02, thus, the time delay is 43^{-11}_{+10} days.

Magnitude shift	0.70 $\pm$0.15 mag
Time delay	43^{-11}_{+10} days

Table 15: The time delay and the magnitude difference estimations from the cross correlation of the linearly interpolated data method.

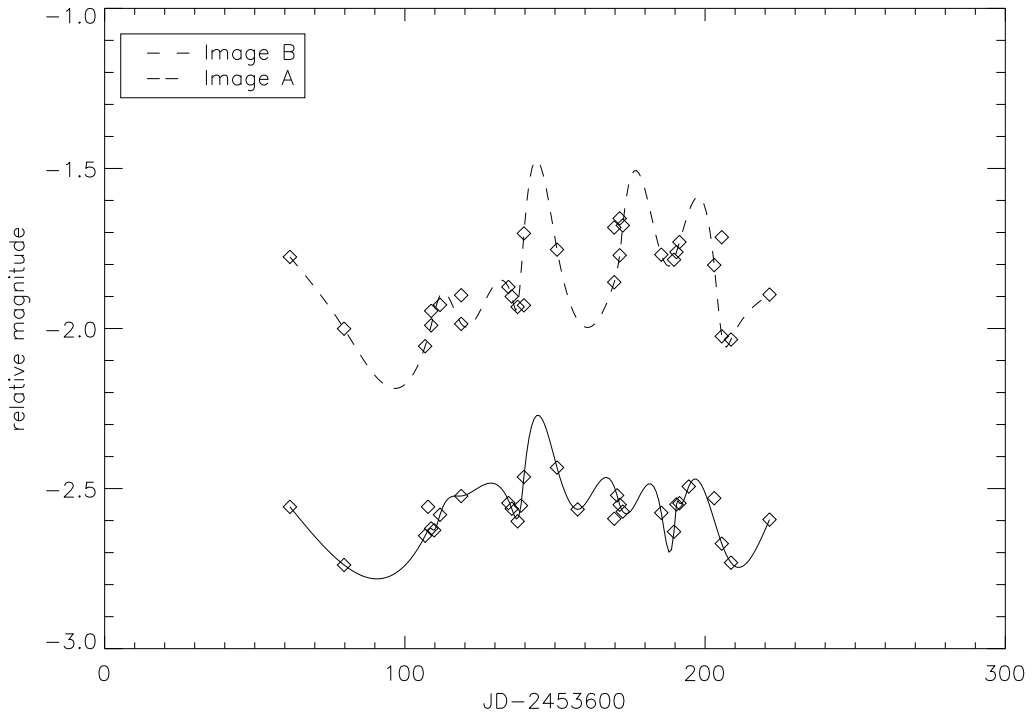

Figure 36: Function fitted to the data of A and B images. We have been looking for the function which fits to the maximum number of data and which represents the realistic shape of the images light curve. In order to obtain it we had to skip the three data points in the B image and one in the image A which were giving high and sharp picks in the fitted light curves.

The Figure 35 presents the light curves difference. The B quasar image has been shifted by the magnitude offset and the time delay found in the cross correlation method and it has been linearly interpolated on the A image. On top of the Figure 35 are shown two light paths, where the B image light path is shifted in time and magnitude. On bottom of the Figure 35 is the light curves difference obtained by use of linear interpolation, it presents the variations due to photometric and interpolation errors or/and possible microlensing signal.

The presented method can be improved by changing the linear interpolation between data into interpolation of functions fitted to the data. On the Figure 36 are presented the fitted functions. We have been looking for the function which fits to the maximum number of data and which represents the realistic shape of the images light curve.

In order to obtain it we had to skip the three data points in the B image and one in the image A which were giving high and sharp picks in the fitted light curves.

On the Figure 37 are shown the results of interpolation between functions representing the light paths of A and B quasar images. On the top plot we see the results of the cross correlation obtained by the linear interpolation between the data and on the bottom plot we see the results of the cross correlation between functions.

We see that this time the cross correlation has its minimum more flat and its center is at the 40 days with the 0.9 magnitude shift. In this case we can assume that the possible time delay range is for up to 0.05 mean light curve difference, thus, the estimated time delay is 40^{-12}_{+13} days (see Table 18).

Magnitude shift	0.90 $\pm$0.15 mag
Time delay	40^{-12}_{+13} days

Table 16: The time delay and the magnitude difference estimations from the cross correlation method of the fitted function.

5.3.1 Time delay summary

Let us summarize what we have learned from the light paths analysis. We have used the three methods for estimating the time delay, two from the light curves analysis and one theoretical. The results of all the methods are gathered in Table 17. We see that the results of the time delay obtained by those four methods are consistent. On Figure

Methods	Time delay
Theoretical	46^{-18}_{+18} days
By eye	30–50 days
Cross correlation of data	43^{-11}_{+10} days
Cross correlation of fitted functions	40^{-12}_{+13} days

Table 17: Time delay estimations results

38 we see that the light curves of the two quasar images with one of them being shifted by the average of the time delay obtained using both mathematical and theoretical methods.

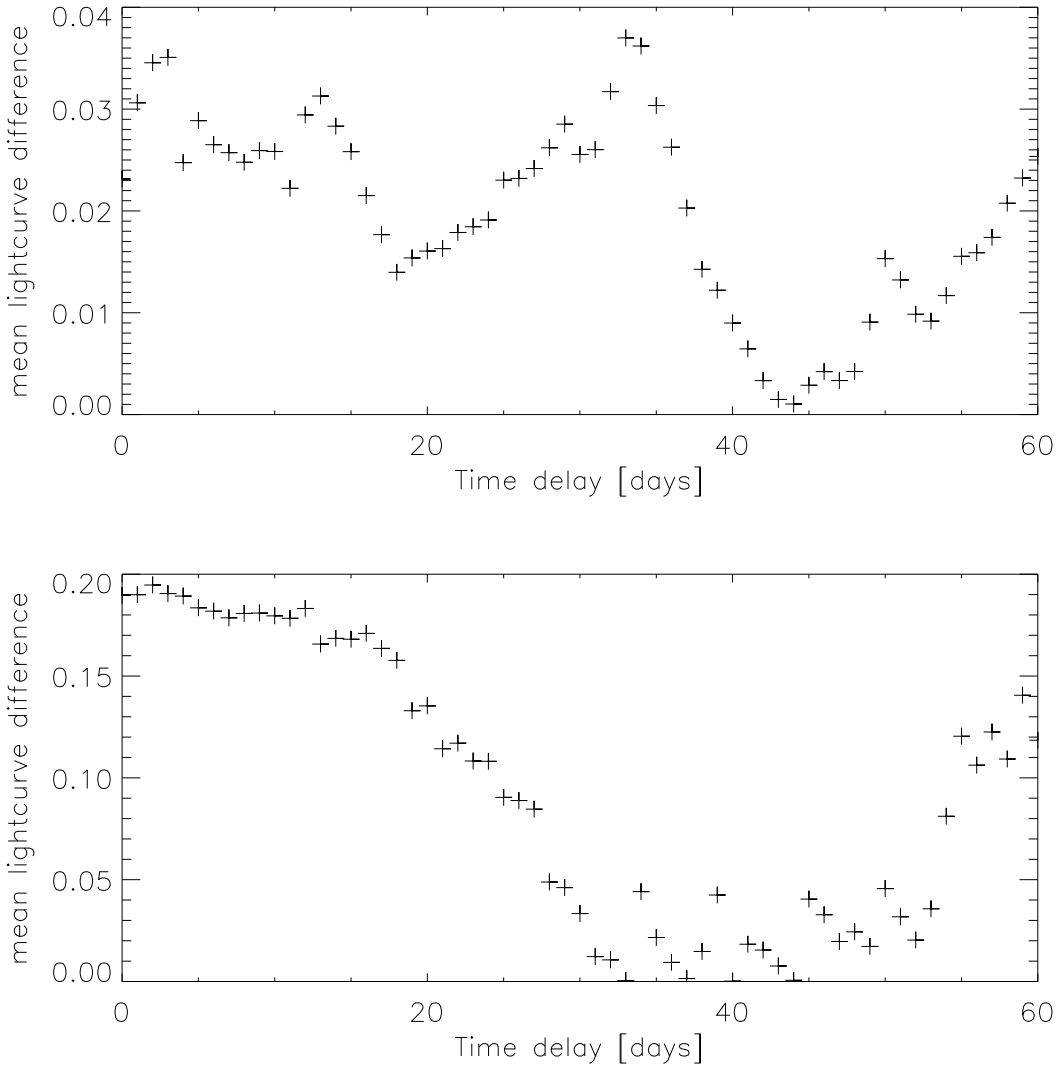

Figure 37: Here is shown the result of the interpolation between the functions representing the light paths of A and B quasar images. On the top plot we see the results of the cross correlation obtained by the linear interpolation between the data and on the bottom plot we see the results of the cross correlation between the functions. We see that the cross correlation has its minimum flat and its center is at the 40 days with the 0.9 magnitude shift.

5.4 Nova

In the night of 28'th January 2006 we have detected a new object which was placed next to the PSF-star on the StanCam images. Because of the bad weather conditions,

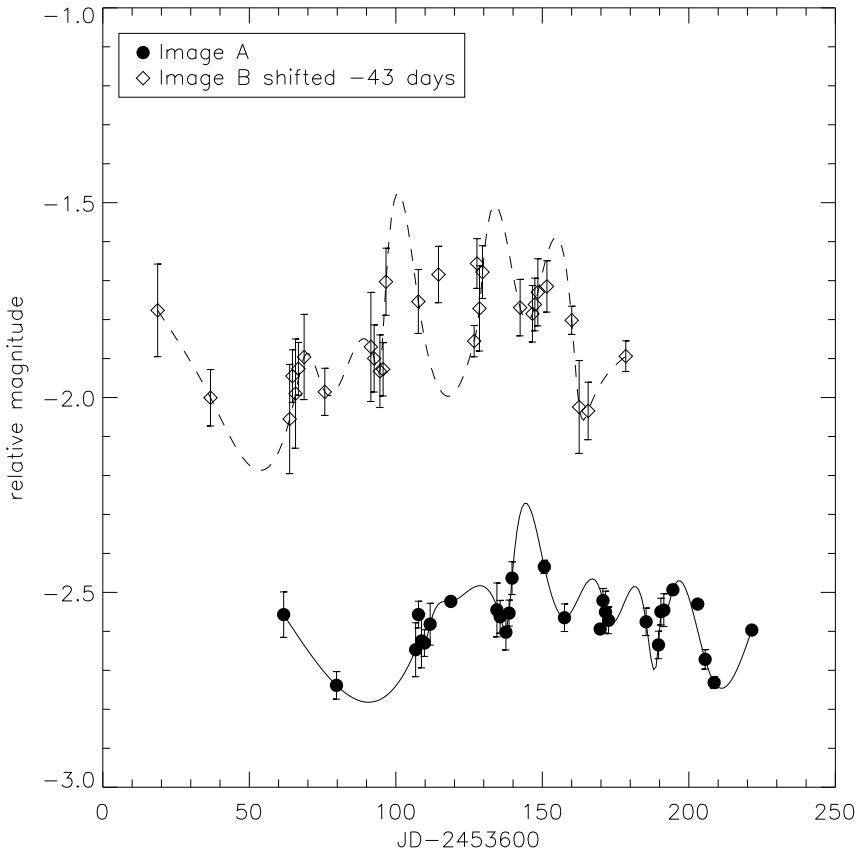

Figure 38: On the Figure we see the light curves of the two quasar images with one of them being shifted by the average of the time delays obtained using both mathematical and theoretical methods.

we have gather only five data points of the object (see Figure 39). During a week of observations we have detected constant demagnification of the object. The first four frames on the Figure 39 present the StanCam observations of the object, the fifth image shows the ALFOSC observation one week after first detection.

Object	R.A.	Decl.	r mag max	r mag
Novae	09 03 23.74	+50 28 47.0	20.99±0.05	25.0±0.1

Table 18: Astrometric and photometric results

We have measured that the observed object is separated by 1.″59 form the star J090343.12+502900.9 and it is positioned R.A.: 09 03 43.03 and Decl.: +50 29 02.22.

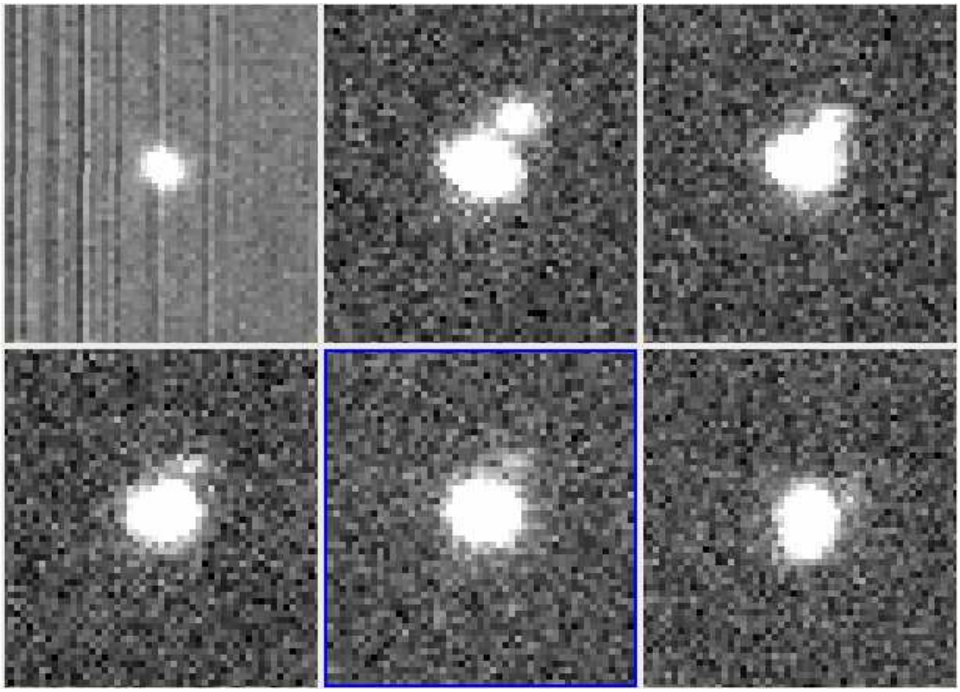

Figure 39: The first four frames on the Figure present the StanCam observations of the object, the fifth image shows the ALFOSC observation one week after first detection.

The brightness in the R-band during the maximum brightness reaches 20.99 mag.

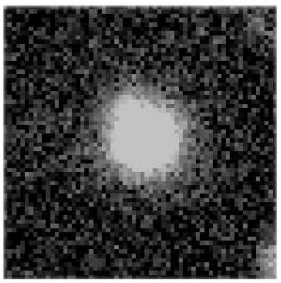

Figure 40: The combination of 16 frames obtained with the ALFOSC camera where the new star is visible, it is aligned above and on the left from central star.

Figure 40 shows the combination of 16 frames obtained with the ALFOSC camera where the new star is visible. Using the aperture photometry we have estimated that the object before the explosion had brightness 25 magnitudes. Thus, the outburst of the object was over 5 mag.

The preliminary results introduced here, the length and the strength of the explo-

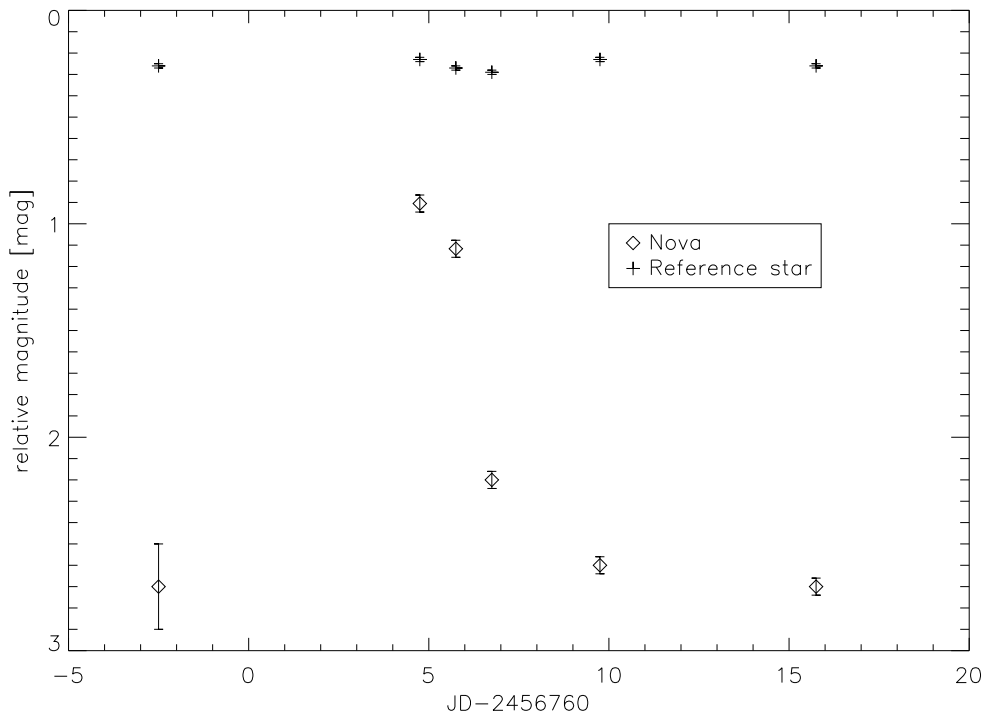

Figure 41: Light curve of the outburst of the observed object. The shape of the light curve indicates that the object is a nova. The first data point of the light curve of the nova is for comparison. It is an artificially added point showing the data of the last observation before an outburst and ah estimated brightness of the object. It shows that a week before an outburst the object was still not visible in our observations.

sion, indicate that the observed outburst was the explosion of a nova. A nova outburst is the consequence of the accretion of hydrogen rich material onto a white dwarf and is the largest hydrogen powered explosion in the Universe. The fuel is supplied by the secondary star in a close binary system while the strong electron degeneracy of the massive white dwarf acts as a container for the gas during the early stages of the explosion (see Warner).

6 Summary and Future research

6.1 Summary

This master thesis contained the theoretical description of up to date knowledge about the strong gravitational lensing (Chapter 2 and 3) and the two practical subjects microlensing (Chapter 3) and the time delay estimation (Chapter 5). In the theoretical part we have introduced the strong lensing theory from both sides, the time delay estimation and the microlensing. In the time delay part we showed how to calculate a mass of a lens from quasar images positions, how to model a mass distribution and explained what is causing delay between images. From the microlensing part, first, we have been presenting the physical properties of a quasar, how to extract a microlensing signal in quasar images light curves and how microlensing affects spectra. This theory was partially applied into the practical parts of the thesis.

In the microlensing subject we searched for the possible microlensing effects in the light curves of the five gravitationally lensed systems. The microlensing research gave as positive results in the two out of the five investigated quasars. We showed that in the quasars SBS 1520+530 and FBQ 0951+2635 exist long and short therm magnitude variations that may be attributed to the microlensing.

The second subject, the time delay estimation in the gravitationally lensed quasar also succeeded. In order to find the time delay of the gravitationally lensed quasar SDSS J0903+502 we made everyday observations at the Nordic Optical Telescope for half year. The observations gave as well sampled data of the quasar.

After the mathematical improvement of the images resolution, we obtained the separate quasar images and the lensing galaxy, which were used for the lensing modeling. Applying the Singular Isothermal Sphere model of the lens we calculated the theoretical time delay of the system 46^{-18}_{+18} days.

We also obtained the light curves of the two quasar images. Using three different methods we estimated the time delays which were coherent with the theoretical prediction. Method by eye gave the result: 30–50 days, cross correlation of data: 43^{-11}_{+10} days and cross correlation of fitted functions: 40^{-12}_{+13} days.

During observation of the quasar images we also detected the outburst of the new object in the StanCam field. Because of the light curve of the outburst (fast brightening , slow fainting) and strength of the explosion (5 mag) we claimed that this object is possibly a nova.

6.2 Future research

This thesis is a beginning of the work that can be done on the subject. All the theory which was presented in the first part of the thesis can be applied into research.

In the microlensing part we were considering simply the microlensing as an event of lensing by an object in a foreground galaxy. As it is described in section 3.4 such an microlensing event is much more complicated. Thus, to improve the microlensing research on the presented quasars we should use one of the techniques described in section 3.4 in order to track the truth quasar light path considering a possible mass distribution in lensing galaxy.

It would be also useful to observe the quasar images spectra to confirm microlensing signal and search for the possible galactic extinctions.

In the time delay part we should analyze more complicated mass models. It should be consider a Singular Isothermal Sphere model with an external shear, which in the case of the SDSS J0903+502 quasar is reasonable, since there are two other galaxies next to the main lensing galaxy.

We should also make longer observing run of the SDSS J0903+502 quasar with similar sampling in order to obtain longer light curves and find more precise time delay of the system.

7 Acknowledgments

I am grateful to my supervisor, who supported me all the time with lots of good advices, good humor, good will and strong believe in my success despite all mistakes I have done.

I am grateful for very efficient knowledge support to my Icelandic friends Palli and Árdís. Additional thanks to Pallé for his Icelandic deconvolution manual and for answering on all mails titled "Deconvolution".

Apology for questions harassment and thanks for tremendous scientific help to all NOT staff especially to Tapio Purismo, Amanda Dupnovnik, Graham Cox and Thomas Augustain, also thanks for the moral support from the rest of the NOT staff.

To make the acknowledgment more private and meaningful I will thanks to my family in their languages. *Dziekuję Mamo bardzo za to, że pomogłaś mi sięgnąć do gwiazd, ta magisterka jest nasza wspólna.*

References

Abajas, C., Mediavilla, E., Muñoz, J.A., Popović,L.Č. Mem. S.A.It. 7,48

Bolton, J. G., Gardner, F. F.& Mackey, F. B. 1963, Natur, 199, 682

Burud, I., Hjorth, J., Jaunsen, A. O., et al. 2000, ApJ, 544, 117

Burud, I., Hjorth, J., Courbin, F., et al. 2002, A&A, 391, 481

Burud, I., Courbin, F., Magain, P., et al. 2002, A&A, 383, 71

Cardelli,J. A., Clayton, G. C. & Mathis, J. S. 1989, ApJ, 345, 245

Chang, K., & Refsdal, S. 1979, Nature, 282, 561

Dressler, A., Lynden-Bell, D., Burstein, D., et al. 1987, ApJ, 313, 42

Einstein, A. 1915, Sitzungber. Preuß. Akad. Wissensch., erster Halbband, p.831

Elvis 2000, ApJ, 545, 63

Elíasdóttir, A. Hjorth, J. Toft, S., Burud, I., Paraficz, D. 2006,

Falco E. E., et al 1999, ApJ, 523, 617

Fomalont, E.B. & Sramek, R.A. 1975, Ap. J., 199, 749

Freedman, P.J., Hawett, P.C., Foltz, C.B., et al., 1998 astro-ph/9801080

Gil-Merino, R. & Lewis, G. F. 2005, A&A 2237

Hjorth, J., Burud, I., Jaunsen, A. O., et al. 2002, ApJ, 572, 11

Hubble, E. P. 1929, Astronomical Society of the Pacific Leaflets, Vol. 1, p.93

Irwin, M. J., Webster, R. L., Hewett, P. C., et al. 1989, AJ, 98, 1989

Johnston, D.E., Richards, G.T., Frieman, J.A., et al. 2003, AJ, 126, 2281

Kayser, R. , Refsdal, S. & Stabell, R., 1986 A&A, 166, 36

Kochanek, C. S. 2004, ApJ, 605, 58

Kochanek, C.S. 1996, ApJ, 473, 595

Kundic, T., Turner, E. L., Colley, W. N., et al. 1997, ApJ, 482, 75

Laplace, P.S. 1795

Madore, B. F. & Freedman, W. 1991 PASP, 103, 933

Magain, P. Courbin F & Sohy, S. 1998, ApJ, 494, 472

Myers, S. T., Baker, J. E., Readhead, A. C. S., et al. 1997, ApJ, 485, 1

Nadau, D., Yee, H. K. C., Forrest, W. J., et al. 1991, ApJ, 376, 430

Ohanian, C. H. 1983, ApJ, 271, 551

Udalski, A. 2003, ApJ, 590, 284

Paczynski, B. 1986, ApJ, 301, 503

Pedersen, K., Rasmussen, J., Sommer-Larsen, J., et al. 2006, NewA, 11, 465

Pelt, J., Schild, R., Refsdal, S., et al. 1998, A&A, 336, 829

Perlmutter, S.,Gabi, S., Goldhaber, G., et al. 1997, ApJ, 483, 565

Phillips, M. M., Phillips, A. C., Heathcote, S. R., et al. 1987 PASP, 99, 592

Refsdal, S. 1964, M.N.R.A.S., 132, 101

Refsdal, S. 1966, MNRAS, 134, 315

Reichard et al. 2003, AJ, 126, 2594

Soldner, J. 1804, Berliner Astron. Jahrb. 1804, 161

Schechter, P. L. 1976, ApJ, 203, 297

Schechter, P. L., Bailyn, C. D., Barr, R., et al. 1997, ApJ, 475, 85

Schechter, P. L. & Kochanek, C.S. 2003, arXiv:astro-ph/0306040 v1 2 Jun 2003

Schmidt, N. 1963, Natur, 197, 1040

Schneider, P. 1986, ApJ, 300, 31

Schneider, P., Weiss, A. 1988, ApJ, 330, 1

Shapley, H. 1919, JRASC, 13, 438S

Shalyapin, V. N. 1993, ARep, 37, 470

Spergel, D. N., Verde, L., Peiris, H. V., et al. 2003, ApJS, 148, 175

Pursimo, T. 2005, http://www.not.iac.es/instruments/stancam/stancam-bias.html

Tully, R. B. & Fisher, J. R. 1977, A&A, 54, 661

Wambsganss, J. 2000, astro-ph/0010004v1 30 Sep 2000

Wambsganss, J. 1997, MNRAS, 284, 172

Walsh, D., Carswell, R.F. & Weymann, R.J. 1979, Nature, 279,

Warner, B. 1995, cvs, book, W 1995

Wisotzki, L., Wucknitz, O., Lopez, S., et al. 1998, A&A, 339, 73

York, D.G., et al. 2000, AJ, 120, 1579

Young, P. 1981, ApJ, 244, 756

A Hubble constant.

One of the most important application of Gravitational Lensing (GL) in Cosmology is the Hubble constant calculation. Gravitational lensing gives completely independent from other methods estimation of this value which makes GL essential tool in Cosmology. Here it is shown what the Hubble constant is and how to obtain it using simple cosmological laws.

In order calculate the Hubble constant one has to introduce the metric of Universe. This metric calls Robertson-Walker metric.

Robertson-Walker metric

Robertson-Walker metric is a metric of the coo-moving coordinate system in the homogeneous Universe:

$$d\tau^2 = dt^2 - a(t)^2 \left[\frac{dr^2}{1-kr^2} + r^2(d\theta^2 + sin^2\theta d\psi^2) \right] \tag{96}$$

where:

- $a(t)$ – is a time scale factor,
- k – is a curvature factor,
- t – is a time variable,
- θ, ψ and r – are space variables.

The three-dimensional space part in the Robertson-Walker metric has a geometric interpretation, this interpretation depends on the curvature factor, k:

k=+1 The Universe is a hypersphere with the curvature equal to: $1/R^2$

k=-1 The Universe is a pseudo-hypersphere and the curvature is everywhere negative: $-1/R^2$

k=0 The Universe is flat.

Hubble's law

To obtain the Hubble law we take simply the Robertson-Walker metric for a radial movement of light ($d\tau = d\theta = d\psi = 0$) and we integrate it:

$$\int_{t_1}^{t_0} \frac{dt}{a(t)} = \int_0^{r_1} \frac{dr}{\sqrt{1-kr^2}} \tag{97}$$

now we take only the left-hand side and write the following equation:

$$R = \int_{t_1+\delta t_1}^{t_0+\delta t_0} \frac{dt}{a(t)} = \int_{t_1}^{t_0} \frac{dt}{a(t)} = R \tag{98}$$

both sides of this equations are equal to the distance R. After integration and approximation (we assume that at δt_0, a(t) does not change significantly), we obtain:

$$\frac{\delta t_1}{\delta t_0} = \frac{a(t_1)}{a(t_0)} = \frac{\lambda_1}{\lambda_0}. \tag{99}$$

From definition of the redshift $z = (\lambda_1 - \lambda_0)\lambda_1$ and from equation 99 we get:

$$z = \frac{\lambda_1 - \lambda_0}{\lambda_1} = \frac{a(t_0)}{a(t_1)} - 1 = \frac{a(t_0) - a(t_1)}{a(t_1)}.. \tag{100}$$

For close by sources we can, from equation 100, we take only the first order:

$$z \approx \frac{\dot{a}(t_0)}{a(t_0)}(t_0 - t_1) \tag{101}$$

where:

- $\dot{a}(t_0)/a(t_0) = H_0$ is a Hubble constant
- $t_0/t_1 = L$ is a physical distance

Finally we put the last two equations into equation 101 and the Hubble law can be write down in the form:

$$z \approx \upsilon \approx H_0 L \tag{102}$$

From equation 102 we see that the Hubble constant is dimensional parameter that describes the current expansion rate of the Universe. The '0' in the Hubble constant refers to the present epoch. The dimension of H_0 is the inverse of time but conventionally we express it as $\mathrm{kms}^{-1}\mathrm{Mpc}^{-1}$. The Hubble constant is believed to lie somewhere in the range 50-70 $\mathrm{kms}^{-1}\mathrm{Mpc}^{-1}$ but the specific value is uncertain.

B The methods of measuring the Hubble constant

There are two main methods for obtaining Hubble constant, so called standard candle and physical, the gravitational lensing belongs to the second group. Here we present the few methods for obtaining the Hubble constant used by astronomers.

Standard candle method From definition of the Hubble constant we know that having redshift (z) and distance (d) for number of galaxies one can estimate H_0. Whereas redshift can be measured with very good accuracy, distance suffers of many kinds of large errors. Depending on which method we use we can obtain different values of a distance and quite different values of H_0.

There are few standard candle methods all of them relay on the physical relation between a measurable parameter and their absolute magnitude. Knowing the relation one can calculate an absolute magnitude of an object and what follows a distance. A distance can be calculated from the equation:

$$m - M = 5 \log d - 5 \tag{103}$$

where: m is an apparent magnitude, M is an absolute magnitude and L is a distance

Here are explained the four main standard candle methods:

- Cepheids (Madore & Freedman 1991): the stars pulsating with the period correlated with their absolute magnitude, thus, measuring the period one can get absolute magnitude and calculate the distance to the object.
- Supernovae 1a type (Phillips et al. 1987): the results from explosion of white dwarf, the maximum luminosity during explosion is correlated with absolute magnitude.
- Galaxies:
  - Spiral galaxies (Tully & Fisher 1977): here the physical relation is between the total luminosity of spiral galaxies and their maximum rotation velocity, it is called Tully-Fisher relation.
  - Elliptical galaxies (Dressler et al. 1987): the relation is between the stellar velocities dispersion and the intrinsic luminosity. This galaxies occupy a "fundamental plane" where the size of a galaxy is correlated with the surface brightness and the velocity dispersion.
- Surface Brightness Fluctuations (SBF) method (Schechter 1976) – the resolution of stars in galaxies is distance depended. By normalizing the mean flux we can get relative distance to galaxies.

Physical method

The alternative of the Standard Candle methods are so called physical methods.

One of the physical methods is based on CMB observations (Myers 1997). The hot cluster gas Compton scatters the cosmic microwave background (CMB) radiation. This scattering, called the Sunyaev-Zeldovich effect (SZE), is measurable using radio telescopes. The CMB has a temperature of 2.73 K which peaks at a wavelength of around 1 mm. Observations at centimeter wavelengths see the SZE as a reduction in the brightness toward the cluster, as the photons are scattered upward in energy. The observed decrement is proportional to the integrated electron density along the line of sight through the cluster.

The SZE depends linearly on the gas density, and with a different power of H_0, than the X-ray emission, so the two quantities together will yield a measure of both the mass and the angular diameter distance (and thus the Hubble constant) if the cluster depth is the same as the observed angular diameter.

The other physical methods is based on the time delay of a gravitationally lensed quasar. From the definition of the Hubble constant, (equation 5) and from the definition of the gravitational time delay, (equation 53) one can get:

$$H_0 = \frac{(1+z_l)}{\Delta\tau}\frac{\tilde{D}_{\rm LO}\tilde{D}_{\rm SO}}{\tilde{D}_{\rm LS}}\left\{\frac{1}{2}(\theta_1-\beta)^2-\frac{1}{2}(\theta_2-\beta)^2-\psi(\theta_1)+\psi(\theta_2)\right\} \tag{104}$$

where: $\tilde{D} = D/R_{mH}$.

Table 19: The age of the Universe t_0 in Gyr for various values of the Hubble constant H_0, the mean matter density Ω_Λ and cosmological constant Ω_m

H_0	Ω_m	Ω_Λ	$t_0(Gyr)$
50	1	0	13
50	0.3	0	15.8
50	0.3	0.7	18.8
60	1	0	10.9
60	0.3	0	13.2
60	0.3	0.7	15.7
70	1	0	9.3
70	0.3	0	11.3
70	0.3	0.7	13.5

C Lensing theory

First, let us assume that lens has a spherically symmetric metric (this situation is showed on the Figure 42). Using this metric in the Einstein equation one can obtain Schwarzschild metric, which is a description of spherically symmetric gravitational field.

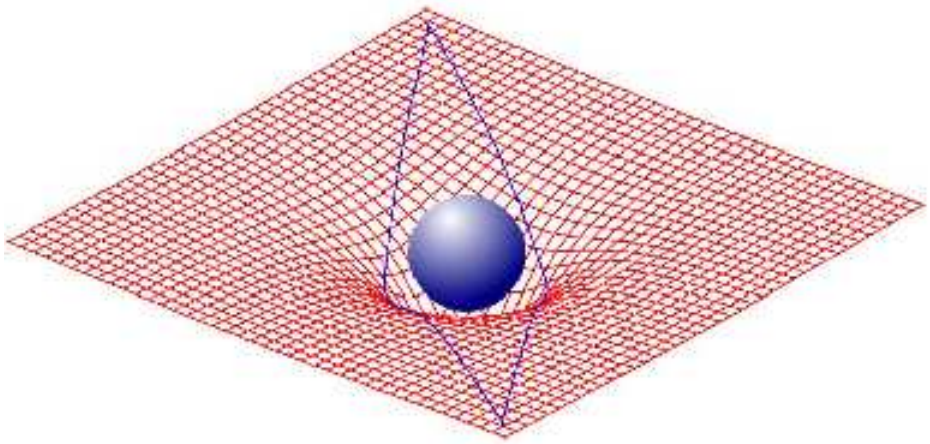

Figure 42: Deflected light beam and geodesic lines of space time near massive object

Procedure to obtain an equation for light deflection is following:

Schwarzschild metric in plane has a form:

$$ds^2 = (1 - \frac{2MG}{r})dt^2 - (1 - \frac{2MG}{r})^{-1}dr^2 - r^2 d\phi^2 \tag{105}$$

where: r, ϕ are space variables, t is a time variable, M is a mass of a deflector and G is the gravitational constant.

Equations of motion. To obtain path of light in the Schwarzschild metric we use the equation of a motion:

$$\frac{d}{dt}\frac{\partial}{\partial p}F = 0 \tag{106}$$

where p is a variable and F is a functional given by equation:

$$F = \frac{ds^2}{d\lambda^2} = (1 - \frac{2MG}{r})\dot{t}^2 - (1 - \frac{2MG}{r})^{-1}\dot{r}^2 - r^2\dot{\phi}^2 = 0 \tag{107}$$

where: $\dot{t} = \frac{dt}{d\tau}$, $\dot{r} = \frac{dr}{d\tau}$ and $\dot{\phi} = \frac{d\phi}{d\tau}$ (here we used the mathematical trick: we can not divide equation 16 by $d\tau$ because for the light $d\tau = 0$, so instead we divide

it by factor $d\tau/d\lambda$). One can easily see that functional F is just a Schwarzschild metric divided by $d\tau/d\lambda$. Now we put F, from the equation 107, to equation of motion 106, and we get:

$$\frac{d}{d\lambda}\frac{\partial}{\partial\dot{\phi}}(\frac{ds}{d\lambda})^2 = 0 \tag{108}$$

$$\frac{d}{d\lambda}\frac{\partial}{\partial\dot{t}}(\frac{ds}{d\lambda})^2 = 0 \tag{109}$$

From integration of equation 108 we get:

$$r^2\dot{\phi}^2 = J \tag{110}$$

and from integration of equation 109 we get:

$$(1 - \frac{2MG}{r})\dot{t}^2 = A = 0 \tag{111}$$

A and J from equation 110 and 111 are integration constants. In the equation 111 we can write that A=0, because we can always adjust clocks in infinity to satisfy this assumption.

When we put equations 110 and 111 to functional F, (from equation 107), we obtain:

$$\frac{\dot{\phi}}{\dot{r}} = \frac{d\phi}{dr} = \frac{J}{r^2}\frac{1}{\sqrt{1 - \frac{J^2}{r^2}(1 - \frac{2MG}{r})}}. \tag{112}$$

From boundary condition: $r_{\min} = r \Rightarrow \frac{dr}{d\phi} = 0$ we get:

$$J = \frac{r_{\min}}{\sqrt{1 - \frac{2MG}{r_{\min}}}}. \tag{113}$$

To simplify calculation we take new variable:

$$x = \frac{r_{\min}}{r}. \tag{114}$$

We put this variable to equation 112, we integrate it and we get:

$$\phi_{\min} - \phi_{\text{infty}} = \int_0^1 \frac{dx}{\sqrt{1 - x^2 - \frac{2GM}{r_{\min}}(1 - x^3)}}. \tag{115}$$

The equation 115 is a full description of a light path in a spherically symmetric gravitational field for an arbitrary distance from a deflector.

D Source magnification

Lensing changes also an apparent luminosity of a lensed object as a consequence of the distortion (see chapter 2.5.2), although the real surface brightness is not changing by lensing effect. To describe this brightness conservation we have to define following:

Surface brightness $I(\nu)$ – the flux of energy, E, of the given frequency, ν, crossing an unit area, dA, perpendicular to the direction of propagation, per unit time, dt, per unit solid angle, $d\Omega$, per unit frequency interval, $d\nu$:

$$I(\nu) = \frac{dE}{dtdAd\Omega d\nu} \tag{116}$$

Phase-space density $f(\vec{x}, \vec{p}, t)$– the number of photons, N, in a given phase-space volume, $d^3\vec{x}d^3\vec{p}$:

$$f(\vec{x}, \vec{p}, t) = \frac{dN}{d^3\vec{x}d^3\vec{p}} \tag{117}$$

knowing that: $dE = h\nu dN = cpdN$, $d^3\vec{p} = p^2 dp d\Omega$ and $d^3\vec{x} = dAcdt$ we obtain:

$$f(\vec{x}, \vec{p}, t) = \frac{dE}{hcp^3 d\nu d\Omega dAdt} = \frac{I(\nu)}{hcp^3} \tag{118}$$

According to Liouville theorem, the phase-space density of photon beam is changing only if absorption or emission appear. Thus, if there is no absorption or emission and Universe expansion can be neglected, then the brightness is conserved.

Brightness conservation in expanding Universe has form:

$$I(\nu) = \frac{I(\nu(1+z))}{(1+z)^3} \tag{119}$$

where:

- z – redshift
- $I(\nu)$ – a flux in the given frequency, ν

E A&A publication

A&A 455, L1–L4 (2006)
DOI: 10.1051/0004-6361:20065502

Astronomy & Astrophysics

LETTER TO THE EDITOR

Microlensing variability in time-delay quasars⋆

D. Paraficz[1,2], J. Hjorth[1], I. Burud[3], P. Jakobsson[1], and Á. Elíasdóttir[1]

[1] Dark Cosmology Centre, Niels Bohr Institute, University of Copenhagen, Juliane Maries Vej 30, 2100 Copenhagen, Denmark
e-mail: danutas@astro.ku.dk
[2] Nordic Optical Telescope (NOT), Apartado 474, 38700 Santa Cruz de La Palma, Canary Islands, Spain
[3] Norwegian Meteorological Institute, PO Box 43, Blindern, 031 3 Oslo, Norway

Received 26 April 2006 / Accepted 15 May 2006

ABSTRACT

We have searched for microlensing variability in the light curves of five gravitationally lensed quasars with well-determined time delays: SBS 1520+530, FBQ 0951+2635, RX J0911+0551, B1600+434 and HE 2149−2745. By comparing the light curve of the leading image with a suitably time offset light curve of a trailing image we find that two (SBS 1520+530 and FBQ 0951+2635) out of the five quasars have significant long-term (∼years) and short-term (∼100 days) brightness variations that may be attributed to microlensing. The short-term variations may be due to nanolenses 10^{-4}−10^{-3} $M_{\odot}$, relativistic hot or cold spots in the quasar accretion disks, or coherent microlensing at large optical depth.

Key words. gravitational lensing

1. Introduction

The effect of a background source being gravitationally lensed by foreground compact objects is known as microlensing. Chang & Refsdal (1979) predicted that in lensed quasar systems the light path should be affected by stars in the lensing galaxy. Moving compact objects in the lensing galaxy can cause spectral changes, brightness variability and, in the case of multiple images, flux ratio anomalies in the lensed quasar. When the foreground galaxy causes multiple images of the quasar, photometric monitoring can be used to isolate intrinsic quasar variability from microlensing variability by comparison of the separate light curves. Likewise, spectral differences between quasar images, caused by differential magnification across the quasar, can be directly detected in multiply imaged quasars. Microlensing offers the opportunity to study the nature of matter in foreground galaxies and the spatial structure of the lensed quasar at very high angular resolution (Kochanek 2004). The first quasar microlensing events were discovered 17 years ago by Irwin et al. (1989) and Schild (1990).

In this Letter we analyze the light curves of five lensed quasars for which a time delay has previously been measured in dedicated monitoring campaigns (Burud et al. 2000, 2002a,b; Hjorth et al. 2002; Jakobsson et al. 2005). Four of them were observed at the Nordic Optical Telescope (NOT) between 1998−2002 and one (HE 2149−2745) was observed at the Danish 1.5-m telescope. We here examine the light curves for microlensing variability and at the same time make all data points available online at the CDS.

⋆ Tables 3–8 are only available in electronic form at the CDS via anonymous ftp to cdsarc.u-strasbg.fr (130.79.128.5) or via http://cdsweb.u-strasbg.fr/cgi-bin/qcat?J/A+A/455/L1

2. Analysis

The images of a lensed quasar may vary due to intrinsic quasar brightness changes and/or microlensing. Microlensing affects the light paths of each image differently (in the simplest case only one path is affected) whereas the intrinsic variations show up in all the images but at different times due to the time delay. Therefore, one can isolate the microlensing signal by calculating the difference between two light curves, suitably shifted in time to correct for the time delay.

Observationally, quasar light curves suffer from sampling effects leading to a need for interpolation. Due to their small separations and the presence of the lensing galaxy they may also potentially be affected by systematic errors in the photometry. To eliminate artifacts arising from such effects we do not interpolate data points with a gap bigger then a time delay of a system and we require that the light curve difference be (1) uncorrelated with the quasar variations and (2) independent of which image light curve we interpolate. These are conservative criteria for detection of a microlensing signal in the light curves which ensure that the signal is reliable and robust. If the criteria are violated the variability may be the result of observational, systematic or interpolation errors.

3. Results

Were we apply the analysis to the five quasar light curves to search for microlensing events.

3.1. SBS 1520+530

The doubly imaged quasar SBS 1520+530 (see Table 1) was monitored between February 1999 and May 2001 at the NOT. In Fig. 1 we show the light curves of the two images, A and B, where B has been shifted in both time (−130 days) and

Table 1. Properties of the lens systems. The time delays were obtained by: 1. Burud et al. (2002b), 2. Jakobsson et al. (2005), 3. Burud et al. (2002a), 4. Hjorth et al. (2002), 5. Burud et al. (2000).

Name	z_l	z_s	Δt (days)	Separation	Ref.
SBS 1520+530	0.72	1.86	130 ± 2	1.57″	1
FBQ 0951+2635	0.24	1.25	16 ± 2	1.10″	2
HE 2149−2745	0.495	2.03	103 ± 12	1.70″	3
RX J0911+0551	0.77	2.80	146 ± 4	3.10″	4
B1600+434	0.41	1.59	51 ± 2	1.38″	5

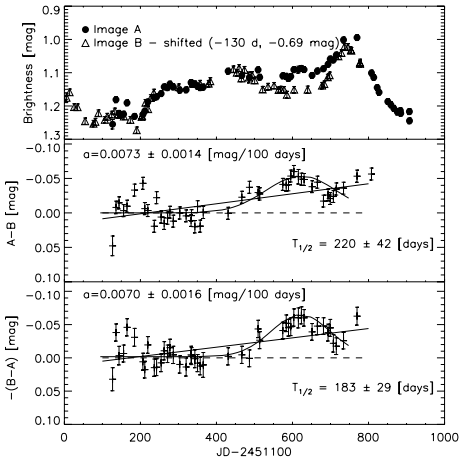

Fig. 1. *R*-band light curves of SBS 1520+530. *Top*: time-delay shifted light curves, with the B image offset by −0.69 mag and −130 days. *Middle*: difference between linearly interpolated A image and B image. *Bottom*: difference between linearly interpolated B image and A image. The middle and bottom panels also present linear fits (where a is the slope) and Gaussian fits (where $T_{1/2}$ is the *FWHM*) to the data.

brightness (−0.69 mag). Also shown are the magnitude residuals, Δm, obtained by linear interpolation of one of the images. The middle panel shows the difference between a linearly interpolated A light curve and the B data points ($\Delta m_{\rm AB}$). The lower panel shows the difference between a linearly interpolated B light curve and the A data points ($\Delta m_{\rm BA}$). Any deviation from a constant difference lightcurve (dashed horizontal line) can be attributed to microclensing. In both residual plots one notices a constant magnitude increase and an approximately 200-day-wide magnitude bump. In the following we characterize such residuals phenomenologically using linear or Gaussian fits.

A linear fit shows that the slopes of the plots are 0.0073 ± 0.0014 mag/100 days for $\Delta m_{\rm AB}$ and 0.0070 ± 0.0016 mag/100 days for $\Delta m_{\rm BA}$. The agreement between these values indicates that the mean difference between the images increases by about 0.007 mag per 100 days. This is consistent with the observations of Gaynullina et al. (2005) who found an increase in the magnitude difference between the quasar images of 0.14±0.03 mag over 1500 days (0.009±0.002 mag/100 days). We interpret this signal as evidence for microlensing.

A Gauss function with baseline zero, fitted to the bump for $\Delta m_{\rm AB}$ gives a *FWHM* of 220 ± 42 days and a peak magnitude variation of 0.053 ± 0.008 mag. For $\Delta m_{\rm BA}$ the *FWHM* is 183 ± 29 days and the peak magnitude variation is 0.063 ± 0.009 mag. These values are consistent within the errors.

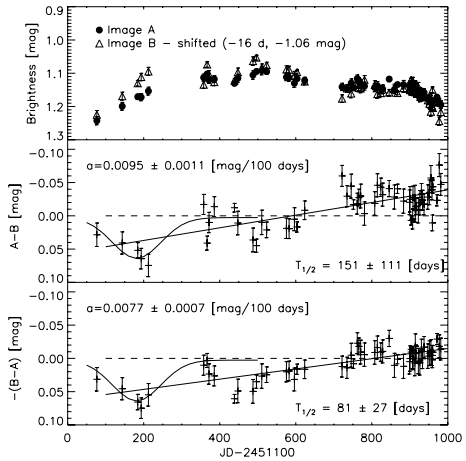

Fig. 2. *R*-band light curves of FBQ 0951+2635. *Top*: time-delay shifted light curves, with the B image offset by −1.06 mag and −16 days. *Middle*: difference between linearly interpolated A image and B image. *Bottom*: difference between linearly interpolated B image and A image. The middle and bottom panels also present linear fits (where a is the slope) and Gaussian fits (where $T_{1/2}$ is the *FWHM*) to the data.

Microlensing in SBS 1520+530 was already detected spectroscopically by Burud et al. (2002b) who analyzed continuum normalized spectra and showed that the equivalent widths of emission lines in A were larger than in B.

3.2. FBQ 0951+2635

The doubly imaged quasar FBQ 0951+2635 (see Table 1) was observed between March 1999 and June 2001 at the NOT. Spectroscopic indications of possible microlensing in the system were found by Schechter et al. (1998) and Jakobsson et al. (2005).

We repeat the microlensing-extraction procedure described above for FBQ 0951+2635. In Fig. 2 we show the light curves of the two images, A and B, the latter shifted in time by −16 days and in brightness by −1.06 mag. The middle and lower panels show $\Delta m_{\rm AB}$ and $\Delta m_{\rm BA}$. In both plots one notices a constant magnitude increase and a bump at the beginning of the observations.

Linear fits to the data yield slopes of 0.0095 ± 0.0011 and 0.0077 ± 0.0007 mag/100 days for $\Delta m_{\rm AB}$ and $\Delta m_{\rm BA}$ respectively. A Gauss function with baseline zero, fitted to the bump for $\Delta m_{\rm AB}$ gives a *FWHM* of 151±111 days and a peak magnitude variation of 0.048 ± 0.009 mag. For $\Delta m_{\rm BA}$ gives *FWHM* of 81 ± 27 days and a peak magnitude variation of 0.061 ± 0.016 mag. These values are consistent within the errors.

3.3. Quasars where no microlensing is confirmed

The three quasars where no microlensing variability was reliably detected are the double quasar HE 2149−2745 observed at the Danish 1.5-m telescope, ESO-La Silla (October 1998−December 2000), the quadruple quasar RX J0911+0551 observed at the NOT (March 1997−April 2001), and the doubly imaged quasar B1600+434

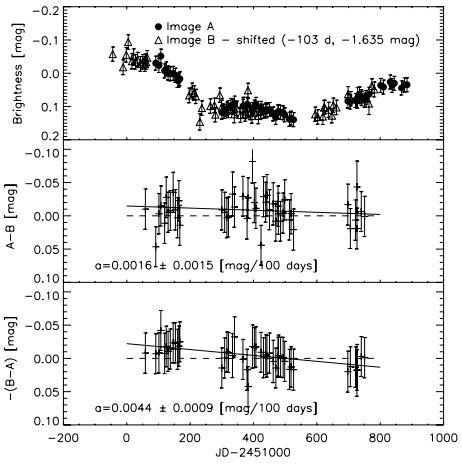

Fig. 3. *V*-band light curves of HE 2149−2745 and the shifted light curve differences. The middle and bottom panels include linear fits with a being the slope of the linear fit.

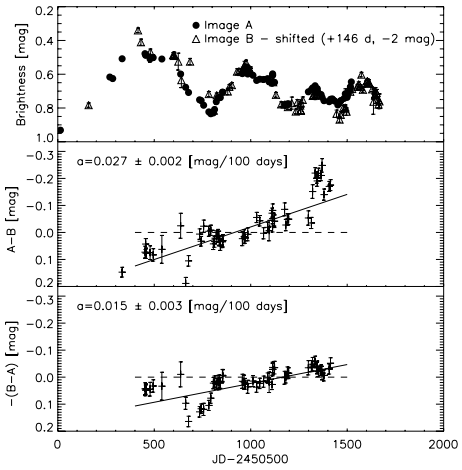

Fig. 4. *I*-band light curves of RX J0911+055 and the shifted light curve differences. The middle and bottom panels include linear fits with a being the slope of the linear fit.

observed at the NOT (April 1998−November 1999) (see Table 1).

Plots similar to Figs. 1 and 2 are shown in Figs. 3−5. For HE 2149−2745 (Fig. 3) and RX J0911+0551 (Fig. 4) we see some long term variations in the light curve difference but the analysis shows that the slopes differ depending on which of the two light curves are interpolated. In B1600+434 (Fig. 5) one sees clear magnitude variations in the light curve differences but they do not satisfy our second condition for microlensing. By comparison with the top plot we see that they are correlated with the quasar variations (the magnitude bump appears at ∼420 days on all plots).

Thus, while we detect intriguing light curve differences and cannot rule out microlensing variability in these systems, this indicates that the detected magnitude changes may also be attributed to photometric or interpolation errors.

4. Discussion

We have demonstrated the existence of a short-term microlensing variability in the photometric data sets of the two quasar systems SBS 1520+530 and FBQ 0951+2635. Interestingly, microlensing has previously been detected spectroscopically and as flux anomalies in both systems (Burud et al. 2002b; Faure et al. 2002; Schechter et al. 1998; Jakobsson et al. 2005). We note that the time scales of the short-term variability detected in the quasars (50−200 days) is similar to the "90 day" events in QSO Q0957+561A,B (see Schild 1996).

In principle one can calculate the masses of the lenses responsible for the microlensing from the time scales of brightness variations (*FWHM*) and the transverse velocities of the compact objects. An approximate value of the lens mass is given by

$$M \approx \left(\frac{\text{time} \times V_{\rm e}}{R_{\rm E}}\right)^2. \quad (1)$$

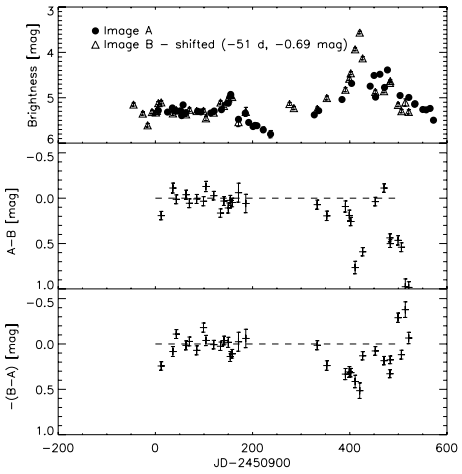

Fig. 5. *I*-band light curves of B1600+434 and the shifted light curve differences.

Here $V_{\rm e}$ is an effective source velocity, defined as the change in time of the source position measured by the observer, and $R_{\rm E}$ is the Einstein radius,

$$R_{\rm E} = \left(\frac{4GM}{c^2}\frac{D_{\rm LS}D_{\rm S}}{D_{\rm L}}\right)^{1/2}, \quad (2)$$

where $D_{\rm LS}$, $D_{\rm S}$ and $D_{\rm L}$ are the lens–source, the source–observer and the lens–observer angular diameter distances, respectively[1].

In Table 2 we show the values of possible microlens masses and the corresponding transverse velocities are given by Eqs. (1)

[1] We assume a flat universe with $\Omega_{\rm m} = 0.3$, $\Omega_\Lambda = 0.7$ and Hubble constant $H_0 = 70\,{\rm km\,s^{-1}\,Mpc^{-1}}$.

Table 2. Mass-speed relation for SBS 1520+530 and FBQ 0951+2635.

Mass	SBS1520+530	FBQ 0951+2635
$[M_\odot]$	Velocity [km s^{-1}]	Velocity [km s^{-1}]
1.0	2.44×10^4	6.87×10^4
0.001	771	2171
0.0001	244	687

and (2). In these calculations we assume that the microlensing is caused by a single compact object. Even with that simplifying assumption, the lens mass can not be determined without knowing the transverse velocity.

There are two possible limits. Due to short duration of the events the microlenses may actually be nanolenses (planets) with masses of order of 10^{-3} $M_\odot$ for typical transverse velocities of the source of 200−700 km s^{-1}. Similar results were obtained for QSO 0957+561 (Pelt et al. 1998). Conversely, fast microlensing variability can be caused by a solar mass object magnifying small continuum parts of the quasar with relativistic velocities (hot spots) (Schechter et al. 2003) or smooth accretion disk occulted by optically-thick, fast moving clouds (Wyithe & Loeb 2002). Applying this to the two quasars, for microlens mass 1 $M_\odot$, we obtain source (hot spot, cloud) transverse velocities of 0.08c for SBS 1520+530 and 0.23c for FBQ 0951+2635.

Because of the mass-velocity degeneracy none of these possibilities can be eliminated from a simple analysis. Moreover, we stress that mass determination using Eq. (1) is only possible for single isolated microlensing events and when the transverse velocity is known. More detailed analyses (Lewis et al. 1993; Wyithe & Turner 2001) assume that the quasar light is affected by numerous compact objects in the foreground galaxy, creating a complex network of caustic lines, and not by a single object (Paczyński 1986).

We conclude that, of the systems we have studied, those with detected flux varability due to microlensing are also reported to have intensity anomalies of spectra continuum and emission line differences. For these systems we have found small linear trends of ∼0.005−0.010 mag/100 days and bumps with amplitude of ∼0.05 mag and durations of ∼100 days. Interestingly, the systems for which no microlensing variability was detected have no convicing detected microlensing from other methods, although there may be indications in e.g. HE 2149−2745 (Burud et al. 2002a). However, smaller microlensing signals (∼0.005 mag/100 days) in these systems would have been undetectable in our observations.

Acknowledgements. We thank Joachim Wambsganss, Rolf Stabell, Cecile Faure and Jaan Pelt for valuable comments. The Dark Cosmology Centre is funded by the DNRF. This work was carried out within the framework of the EC FP6 Marie Curie Research Training Network "Astrophysics Network for Galaxy LEnsing Studies (ANGLES)". D.P. acknowledges receipt of a research studentship at the Nordic Optical Telescope. The data used are based on observations made with the Nordic Optical Telescope, operated on the island of La Palma jointly by Denmark, Finland, Iceland, Norway, and Sweden, in the Spanish Observatorio del Roque de los Muchachos of the Instituto de Astrofisica de Canarias.

References

Burud, I., Hjorth, J., Jaunsen, A. O., et al. 2000, ApJ, 544, 117
Burud, I., Courbin, F., Magain, P., et al. 2002a, A&A, 383, 71
Burud, I., Hjorth, J., Courbin, F., et al. 2002b, A&A, 391, 481
Chang, K., & Refsdal, S. 1979, Nature, 282, 561
Faure, C., Courbin, F., Kneib, J. P., et al. 2002, A&A, 386, 69
Gaynullina, E. R., Schmidt, R. W., Akhunov, T. et al. 2005, A&A, 440, 53
Hjorth, J., Burud, I., Jaunsen, A. O., et al. 2002, ApJ, 572, L11
Irwin, M. J., Webster, R. L., Hewett, P. C., et al. 1989, AJ, 98, 1989
Jakobsson, P., Hjorth, J., Burud, I., et al. 2005, A&A, 431, 103
Kochanek, C. S. 2004, ApJ, 605, 58
Lewis, G. F., Miralda-Escudé, J., Richardson, D. C., et al. 1993, MNRAS, 261, 647
Paczyński, B. 1986, ApJ, 301, 503
Pelt, J., Schild, R., Refsdal, S., et al. 1998, A&A, 336, 829
Schechter, P. L., Gregg, M. D., Becker, R. H., et al. 1998, AJ, 115, 1371
Schechter, P. L., Udalski, A., Szymański, M., et al. 2003, ApJ, 584, 657
Schild, R. E. 1990, AJ, 100, 1771
Schild, R. E. 1996, ApJ, 464, 125
Wyithe, J. S. B., & Turner, E. L. 2001, MNRAS, 320, 21
Wyithe, J. S. B., & Loeb, A. 2002, ApJ, 577, 615

F Observational data

The Table presents details concerning observations carried during October–April 2005. Observations was made by use of the ALFOSC and the StanCam CCD cameras.

Date	Number of images	type of camera	weather condition
22 September 2005	1	ALFOSC	
17 October	1	ALFOSC	full moon
18 October	1	ALFOSC	
28 October	1	ALFOSC	
31 October	1	ALFOSC	
4 November	1	ALFOSC	seeing $>2''$
12 November	1	StanCam	
1 December	1	ALFOSC	
2 December	1	ALFOSC	
3 December	1	ALFOSC	
4 December	1	ALFOSC	
6 December	1	ALFOSC	
29 December	1	ALFOSC	
30 December	1	ALFOSC	
1 January	2	ALFOSC	
2 January	2	ALFOSC	
3 January	2	ALFOSC	
14 January	1	StanCam	
21 January	2	ALFOSC	
29 January	1	StanCam	
30 January	1	StanCam	
31 January	1	StanCam	
1 February	1	StanCam	
2 February	1	StanCam	
3 February	2	ALFOSC	
4 February	2	ALFOSC	
5 February	2	ALFOSC	
13 February	1	StanCam	
17 February	2	ALFOSC	
18 February	2	ALFOSC	
19 February	2	ALFOSC	
20 February	2	ALFOSC	
21 February	2	ALFOSC	
22 February	2	ALFOSC	
23 February	2	ALFOSC	
24 February	2	ALFOSC	
26 February	2	ALFOSC	
02 March	2	ALFOSC	
04 March	2	ALFOSC	
05 March	1	StanCam	
07 March	1	StanCam	
08 March	1	StanCam	
10 March	1	StanCam	
11 March	1	StanCam	
13 March	1	StanCam	
14 March	1	StanCam	

G Informations about the SDSS J0903+502 field

r	RAJ2000	DEJ2000	cl	SDSS	umag	gmag	rmag
arcmin	"h:m:s"	"d:m:s"			mag	mag	mag
			3	J090316.37+503533.7	22.381	22.002	21.177
0.0736	09 03 33.58	+50 28 20.8	3	J090333.57+502820.8	21.642	21.187	20.054
0.0844	09 03 33.47	+50 28 18.4	3	J090333.47+502818.4	19.931	19.499	19.177
0.0916	09 03 34.45	+50 28 22.4	6	J090334.45+502822.4	24.499	22.753	20.875
0.1244	09 03 34.47	+50 28 13.0	3	J090334.47+502813.0	19.341	18.881	18.506
0.1501	09 03 34.94	+50 28 19.4	3	J090334.94+502819.3	19.503	18.720	18.450
0.1773	09 03 35.05	+50 28 15.5	6	J090335.05+502815.5	22.455	22.043	20.807
0.1857	09 03 35.16	+50 28 20.3	3	J090335.16+502820.2	19.904	19.299	18.998
0.1912	09 03 34.97	+50 28 25.8	3	J090334.97+502825.7	20.591	19.862	19.189
0.2802	09 03 35.36	+50 28 08.3	6	J090335.35+502808.2	22.782	22.611	22.338
0.2818	09 03 35.74	+50 28 16.0	3	J090335.74+502816.0	21.798	21.540	21.414
0.2981	09 03 32.90	+50 28 04.5	3	J090332.89+502804.5	21.258	21.108	20.693
0.3061	09 03 32.11	+50 28 15.5	3	J090332.11+502815.5	21.641	22.616	21.795
0.4826	09 03 30.97	+50 28 20.2	3	J090330.96+502820.2	21.757	21.795	20.960
0.5416	09 03 33.40	+50 27 47.0	3	J090333.40+502747.0	22.262	21.484	21.047
0.5633	09 03 30.72	+50 28 31.8	6	J090330.72+502831.7	22.152	21.606	21.491
0.6158	09 03 37.54	+50 28 33.9	6	J090337.54+502833.9	22.015	20.903	20.283
0.6637	09 03 32.74	+50 28 56.9	3	J090332.73+502856.9	21.320	20.902	20.569
0.6737	09 03 38.07	+50 28 30.0	3	J090338.07+502830.0	22.324	22.431	21.457
0.7386	09 03 35.48	+50 29 01.0	6	J090335.47+502901.0	22.194	21.140	20.637
0.7403	09 03 37.92	+50 28 42.9	3	J090337.91+502842.9	22.501	22.435	21.839
0.7414	09 03 30.19	+50 28 44.6	6	J090330.18+502844.6	25.019	25.079	20.907
0.7616	09 03 38.77	+50 28 23.1	3	J090338.76+502823.0	23.097	23.775	21.727
0.7898	09 03 31.57	+50 29 00.3	3	J090331.57+502900.3	22.023	21.599	21.787
0.8356	09 03 29.74	+50 27 49.7	3	J090329.73+502749.6	23.294	22.163	21.501
0.8464	09 03 38.52	+50 27 52.2	6	J090338.52+502752.2	23.003	21.450	21.037
0.8626	09 03 28.58	+50 28 20.1	6	J090328.58+502820.1	23.004	22.049	21.426
0.8801	09 03 29.47	+50 28 49.3	3	J090329.47+502849.3	19.318	18.828	18.476
0.8805	09 03 28.73	+50 28 35.0	3	J090328.72+502835.0	20.104	19.777	19.458
0.9431	09 03 36.32	+50 29 11.1	3	J090336.32+502911.0	23.039	21.887	20.864
0.9472	09 03 31.83	+50 27 26.1	3	J090331.83+502726.0	19.312	18.859	18.507
0.9561	09 03 39.50	+50 27 55.9	6	J090339.49+502755.8	23.986	24.533	20.483
0.9701	09 03 27.99	+50 28 09.2	6	J090327.99+502809.2	21.200	20.017	19.230
1.0008	09 03 32.56	+50 29 17.4	6	J090332.55+502917.4	21.815	21.298	21.104
1.0155	09 03 30.80	+50 27 26.3	3	J090330.79+502726.3	21.518	21.827	22.573
1.0526	09 03 28.11	+50 27 50.2	3	J090328.11+502750.2	22.037	20.605	19.956
1.0584	09 03 27.47	+50 28 31.1	3	J090327.47+502831.1	21.543	20.466	20.011
1.0755	09 03 30.11	+50 29 11.8	3	J090330.11+502911.7	21.419	21.702	24.601
1.0769	09 03 31.53	+50 27 18.8	6	J090331.53+502718.8	23.001	22.134	22.387
1.0906	09 03 33.40	+50 29 24.2	6	J090333.40+502924.1	22.851	22.132	21.073
1.1116	09 03 27.06	+50 28 11.3	3	J090327.06+502811.3	21.881	21.475	21.337
1.1362	09 03 38.22	+50 29 14.0	3	J090338.22+502913.9	22.648	21.928	21.449
1.1601	09 03 37.78	+50 27 19.5	6	J090337.78+502719.4	14.925	14.816	14.837
1.1727	09 03 35.67	+50 27 10.5	3	J090335.67+502710.4	20.475	19.992	19.547
1.1817	09 03 31.66	+50 29 26.3	3	J090331.65+502926.2	22.106	20.867	21.634
1.2020	09 03 30.36	+50 27 15.8	3	J090330.35+502715.8	21.914	20.915	21.731
1.2102	09 03 41.36	+50 28 37.4	3	J090341.35+502837.3	22.574	20.837	20.412
1.2499	09 03 38.71	+50 27 19.0	3	J090338.71+502719.0	22.396	20.794	22.656
1.2597	09 03 26.64	+50 28 46.9	3	J090326.64+502846.8	22.346	21.752	21.922
1.2626	09 03 39.09	+50 29 17.1	6	J090339.09+502917.1	22.533	21.775	21.366